

Journal Pre-proof

Mesoporous Silica as a Tunable Support for Dual-Function Ba–Ru Catalysts: Impact on CO₂ Adsorption and Methanation Performance

S. Molina-Ramirez, G. Nava, E. Finocchio, L. Lietti, L. Viganò, M. Di Virgilio, B. Di Credico, R. Scotti, C. Cristiani, L. Castoldi

PII: S1387-1811(26)00055-7

DOI: <https://doi.org/10.1016/j.micromeso.2026.114080>

Reference: MICMAT 114080

To appear in: *Microporous and Mesoporous Materials*

Received Date: 14 October 2025

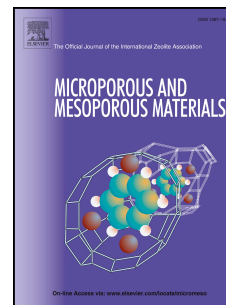
Revised Date: 24 January 2026

Accepted Date: 9 February 2026

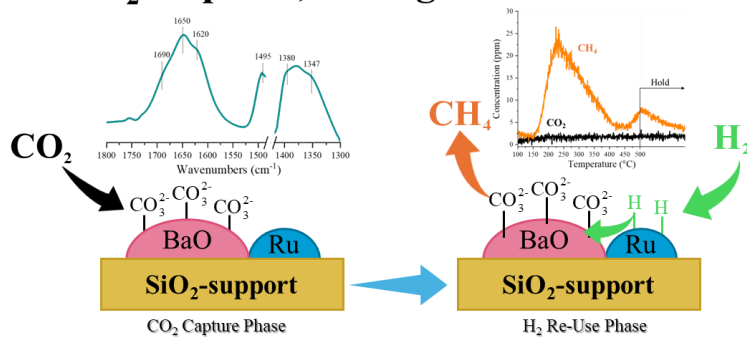
Please cite this article as: S. Molina-Ramirez, G. Nava, E. Finocchio, L. Lietti, L. Viganò, M. Di Virgilio, B. Di Credico, R. Scotti, C. Cristiani, L. Castoldi, Mesoporous Silica as a Tunable Support for Dual-Function Ba–Ru Catalysts: Impact on CO₂ Adsorption and Methanation Performance, *Microporous and Mesoporous Materials*, <https://doi.org/10.1016/j.micromeso.2026.114080>.

This is a PDF of an article that has undergone enhancements after acceptance, such as the addition of a cover page and metadata, and formatting for readability. This version will undergo additional copyediting, typesetting and review before it is published in its final form. As such, this version is no longer the Accepted Manuscript, but it is not yet the definitive Version of Record; we are providing this early version to give early visibility of the article. Please note that Elsevier's sharing policy for the Published Journal Article applies to this version, see: <https://www.elsevier.com/about/policies-and-standards/sharing#4-published-journal-article>. Please also note that, during the production process, errors may be discovered which could affect the content, and all legal disclaimers that apply to the journal pertain.

© 2026 Published by Elsevier Inc.



Graphical Abstract

CO₂ Capture, Storage and Re-Use

Journal Pre-proof

1 Mesoporous Silica as a Tunable Support for Dual-Function Ba–Ru Catalysts:

2 Impact on CO₂ Adsorption and Methanation Performance

3 S. Molina-Ramirez¹, G. Nava², E. Finocchio^{3*}, L. Lietti², L. Viganò¹, M. Di Virgilio¹,

4 B. Di Credico⁴, R. Scotti⁴, C. Cristiani¹, L. Castoldi^{2*}

5 ¹Dipartimento di Chimica, Materiali e Ingegneria Chimica “Giulio Natta”, Politecnico di Milano,
6 Piazza Leonardo Da Vinci 32, Milano, Italy.

7 ²Dipartimento di Energia, Laboratory of Catalysis and Catalytic Processes, Politecnico di Milano,
8 Via la Masa 34, Milano, Italy.

9 ³Dipartimento di Ingegneria Civile, Chimica e Ambientale, Università di Genova (UNIGE),
10 Via all’Opera Pia 15, Genova, Italy.

11 ⁴Dipartimento di Scienza dei Materiali, Università Milano-Bicocca, Piazza dell’Ateneo Nuovo 1,
12 Milano, Italy.

13 *corresponding authors: elisabetta.finocchio@unige.it; lidia.castoldi@polimi.it

14

Abstract

The integration of CO₂ capture and catalytic methanation into a single material platform presents an efficient route toward carbon-neutral fuel production. In this work, we investigate silica-supported dual-function materials (DFMs) comprising Ba as the CO₂ storage component and Ru as the methanation catalyst. A series of Ba-Ru/SiO₂ materials were synthesized via incipient wetness impregnation, with varying Ba loadings (16-32 wt.%) and promoter deposition sequences. Structural, morphological, and surface analyses (BET, XRD, FT-IR) revealed the formation and thermal evolution of distinct carbonate species as a function of Ba content and preparation method. CO₂-TPD and H₂-TPSR experiments demonstrated that the impregnation order influences the nature, strength, and regenerability of the adsorbed carbonate species. Increasing Ba loading enhances CO₂ uptake and promotes the formation of thermally stable bridging carbonates, while Ru positioning affects methanation activity and carbonate reactivity. Compared to alumina-based DFMs, silica-supported systems exhibit distinct carbonate populations and lower-temperature regeneration behavior due to the non-interacting nature of the support. These findings offer new insights into the design of mesoporous DFMs with tunable CO₂ sorption and conversion performance, highlighting the properties of silica as support for integrated carbon capture and utilization.

31

32

33

34

35

36

37

38

Keywords: Silica; FT-IR spectroscopy; DFM; CO₂ capture and Utilization; Barium; Ruthenium

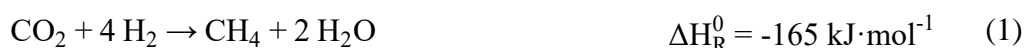
40

41 1. Introduction

42 The rising concentration of atmospheric CO₂ [1], mainly caused by anthropogenic CO₂ emissions
43 from the power generation and industry sectors [2], is producing serious environmental impacts. To
44 mitigate this issue, two main strategies are typically considered: replacing fossil fuels with synthetic
45 fuels produced using green H₂, and capturing CO₂ from the environment. In this context, CO₂ capture
46 is expected to play a larger role because it can be integrated into already existing industrial processes,
47 and is considered more cost-effective than switching entirely to green fuels, also given the limited
48 availability of large amounts of renewable energy.

49 Several approaches for the mitigation of atmospheric CO₂ have been proposed, including the capture
50 from point-source emissions or from the environment, also known as Direct Air Capture (DAC) [3].
51 Despite the difference in CO₂ level – respectively about 10-16% [4] vs 420 ppm] [5] - both imply the
52 absorption of CO₂ utilizing liquid solvents, principally amines [6], or the adsorption of CO₂ utilizing
53 solid sorbents, such as zeolites or metal oxides [7,8] which rely respectively on physisorption and
54 chemisorption.

55 The captured CO₂ is then released through temperature or pressure swings, resulting in a concentrated
56 CO₂ stream that can be injected under the ground (Carbon Capture and Storage, CCS) or utilized as
57 feedstock for the production of fuels, chemicals, etc. (Carbon Capture, Utilization and Storage,
58 CCUS). One way to utilize captured CO₂ is to convert it into methane through the Sabatier reaction
59 (Eq.1), employing (green-)H₂:



60 The as-obtained e-Methane has gained interest over the years given by the possibility to easily
61 transport it, store it and use it since the natural gas infrastructure is already present, so that it can be
62 injected into the already existing grids for natural gas and utilised as it is. These considerations make
63 appealing the utilization of e-CH₄ as energy carrier (Power-to-Gas), along with the fact that for the
64 already established methanation process, which is performed by co-feeding stoichiometric amounts

65 of CO₂ and H₂ (split 1:4), modern catalysts and plant configurations enable a CO₂ conversion and
66 methane selectivity both close to 100% (>98% [9]), thus requiring condensation of byproduct H₂O as
67 the only needed downstream operation to obtain a grid-compatible product.

68 The state of the art of methanation catalyst are composed by a hydrogenation metal (Ni, Ru) dispersed
69 over a support (i.e. Al₂O₃, TiO₂, SiO₂, CeO₂). In the literature, the nature of the support has been
70 investigated in relation to the hydrogenation metal activity [10,11], showing that it is strongly related
71 to the support utilized due to electronic or strong metal - support interactions (EMSI or SMSI). Indeed,
72 other than affecting the dispersion and the size of the particles of the catalyst metal, the support
73 actively contributes to the reaction for the adsorption/activation and hydrogenation of CO₂ at the
74 metal - support interface, ultimately modifying the activity and selectivity of the catalytic material.
75 From a process perspective, traditional CO₂ methanation requires two sequential units, dedicated
76 respectively to the separation and purification of CO₂ and to its methanation, resulting in high Capital
77 Expenditure (CAPEX), along with high Operational Expenditure (OPEX) related to the energy
78 intensive nature of both CO₂ capture (need of temperature/pressure swings [12]) and conversion
79 (necessity of heat management of the exothermic reaction).

80 To overcome these criticalities, the integration of these two operations in one single reactor has been
81 proposed exploiting the so-called Dual Function Materials (DFMs) [13,14]. Indeed, in this case a
82 stream containing CO₂ (i.e. flue gas, biogas) passes through the catalyst bed where the CO₂ is
83 adsorbed (likely as carbonates); then, by exposing the same catalytic bed to green H₂, the captured
84 CO₂ is converted into methane. This integration is made possible utilizing a catalyst constituted by a
85 support (metal oxide) impregnated with a storage material, typically an alkali/-earth metal oxide, and
86 a methanation metal (Ni, Ru). The co-presence of the active elements over the same support has been
87 proven to provide beneficial effects towards the formation of active storage sites (i.e., due to the Ru-
88 catalysed decomposition of Na₂CO₃ precursor [15]) or due to intimate contact effects that allow
89 increased CH₄ yields [16,17].

90 Literature research on DFMs has been conducted employing Al_2O_3 as support, mainly due to its great
91 availability and mechanical properties (high surface area, porosity and stability in the range of
92 operation). Arellano-Treviño et al. [18] studied Ni, Ru and Rh as hydrogenation metals identifying
93 Ru as the most promising candidate due to cost effectiveness in comparison with Rh, and reducibility,
94 that ruled out Ni. Indeed, when O_2 is present in the adsorption phase Ni is irreversibly oxidized, so
95 during the subsequent reduction phase the active metallic form has been irretrievably lost. Long term
96 deactivation effects on Ru have been observed by Jeong-Potter et al. [19], reporting irreversible Ru
97 deactivation due to metal sintering after considerable adsorption and reduction cycles. Moreover, they
98 demonstrate that DFMs are able to perform also at Ru loadings as low as 0.5%. The same loss of
99 hydrogenation activity has been observed also by Bermejo-López et al. [20], that reported also the
100 agglomeration of the storage element among the deactivation causes.

101 The nature of the storage element has been proven to significantly effects the reactivity of these
102 materials [21–24]. Porta et al. [22] investigated different alkaline and alkaline-earth metals,
103 concluding that the highest the basicity of storage elements, the higher the stability of the formed
104 carbonates, leading to uncomplete conversion of the adsorbed species in particular for alkaline-earth
105 metals. The presence of more stable carbonates is positive when the catalyst is tested under flue gas
106 conditions, limiting the competitive adsorption of H_2O .

107 Regarding the composition of the feed gas, Porta et al. [25] and Bermejo-López et al. [26] reported
108 that the adsorption of CO_2 is inhibited by the presence of O_2 and NO , due to the increased acidity of
109 the latter which leads to a preferential absorption of NO . Therefore, during the reduction phase small
110 amount of CH_4 are obtained while the production of N-compounds such as N_2 and NH_3 is significant.

111 With the goal of achieving an active and stable formulation, also the effect of the support of DFMs is
112 now starting to attract attention. Several studies of González-Velasco and coworkers [27,28] have
113 explored CeO_2 -supported DFMs, particularly Ni- and Ru- based perovskite formulations, showing
114 that CeO_2 enables smaller metal nanoparticles (Ni [27]), higher CH_4 yields, and better stability than

115 Al₂O₃-based systems, where NiAl₂O₄ formation negatively affects the redox properties of catalyst.
116 Metal-support interactions are likely behind these performance differences. In agreement, Bracciotti
117 et al. [29] observed an increase in activity and stability towards CO₂ hydrogenation of In₂O₃/(CeO₂-
118 ZrO₂) compared to In₂O₃/ZrO₂, due to the formation of Ce-Zr-In interfacial sites that enhance In₂O₃
119 dispersion and inhibit its reduction to metallic In under reaction conditions, possibly due to the
120 oxygen storage capacity provided by Ce⁴⁺/Ce³⁺. Merkouri et al. [30] reported the high activity and
121 selectivity of bimetallic NiRu catalysts supported on CeO₂-Al₂O₃, with near-equilibrium CO₂
122 conversion, 100% CH₄ selectivity at 350 °C and high stability for traditional methanation reaction.
123 Promoting this catalyst with K results in a DFM with enhanced redox and basic properties due to the
124 ceria-based support. These findings underscore the role of the support regarding redox and surface
125 basicity properties, in regulating both the catalytic activity and adsorption capacity of DFMs. In a
126 recent study by Bahrami et al. [31], the optimization of DFMs was significantly advanced. The
127 authors focused on a Na-Ni-Ru system supported on CeO₂-Al₂O₃, using a Gaussian process surrogate
128 model to navigate the complex interplay between adsorbent loading and catalytic activity. While
129 traditional experimental screening of Na loadings (2.5-15 wt%) indicated that higher adsorbent
130 content generally increased CO₂ desorption capacity, it did not linearly correlate with methane yield.
131 The Research Group identified an optimal Na loading of 7.9 wt.%, which achieved a peak methane
132 production of 398.6 μmol/g_{DFM} with the highest selectivity at 400 °C [31].

133 TiO₂ has been examined by Cimino et al. [32], reporting an enhanced Ru activity towards methanation
134 when supported on TiO₂ rather than Al₂O₃ in agreement with the previous literature [33,34]; on the
135 other hand, the introduction of the storage element (Na or Li) on Ru/TiO₂ results in a detrimental
136 methanation activity, consistent with what previously observed for Al₂O₃-based DFMs [35].
137 Moreover, in the case of TiO₂-based DFMs the presence of a storage alkaline metal decreases the
138 selectivity to CH₄ with the respect to analogue Al₂O₃-based DFMs; indeed, the interaction between

139 the storage element and TiO_2 modified the basicity of the material, possibly due to electronic
140 interactions thus modifying the selectivity.

141 Among the other supports, silica (SiO_2) recently has emerged as a widely investigated support
142 material, owing to a combination of physicochemical properties that favour both metal dispersion and
143 stability under reaction conditions. Firstly, silica offers a high specific surface area and a tuneable
144 pore structure, particularly in mesoporous forms. These properties facilitate a high dispersion of
145 active metal sites, such as Ni or Ru [36], and promote efficient mass transport of gaseous reactants
146 and products.

147 Secondly, SiO_2 is chemically inert and thermally stable, which makes it resistant to structural
148 degradation or undesired chemical interactions during long-term operation. This inertness, while
149 generally unfavourable for direct CO_2 activation due to the lack of basic surface sites, is advantageous
150 when used in conjunction with basic promoters such as alkali or alkaline-earth oxides (e.g., MgO ,
151 CaO , BaO) [37]. These additives compensate for the low intrinsic CO_2 affinity of silica by introducing
152 surface basicity, thereby enabling the capture and activation of CO_2 through the formation of
153 carbonate or bicarbonate species.

154

155

156

157

158 Finally, silica is abundant, cost-effective, and compatible with various scalable synthesis methods,
159 making it suitable for industrial catalyst design. Although it lacks the intrinsic CO_2 adsorption
160 capacity of more basic oxides like Al_2O_3 or CeO_2 [38], its modifiability and structural flexibility make
161 it a valuable platform for the development of advanced bifunctional catalysts.

162 For these reasons, in this work the utilization of silica as support for the integrated CO_2 capture and
163 methanation with DFMs is being investigated through microreactor experiments and FT-IR

164 characterization, to evaluate the surface properties of the SiO₂ supported DFMs and describe the
165 chemistry behind their catalytic activity.

166

167 **2. Materials and methods.**

168 *2.1. Catalysts synthesis*

169 The Dual Function Materials (DFMs) have been prepared using commercial silica (BASF, S_{BET} = 360
170 m²·g⁻¹, V_p = 0.83 cm³·g⁻¹) as support. Pellets have been grinded and sieved to obtain a powder having
171 a particle diameter between 75 and 106 μm; the powder is then dried at 120 °C overnight.

172 Incipient wetness impregnation method has been used to prepare Ba-Ru/SiO₂ catalysts. DFMs have
173 been prepared by impregnating via wetness impregnation the dried SiO₂ support with a solution of
174 ruthenium nitrosyl nitrate (Alfa Aesar, commercial solution 1.5% g_{Ru}·mL⁻¹), dosed to obtain a 0.5
175 wt.% of Ru. The obtained material is then dried at 100 °C for 12 h and then calcined at 500 °C for 5
176 h (2 °C·min⁻¹ heating ramp). The so-obtained Ru/SiO₂ sample. has been impregnated with a solution
177 of barium acetate (precursor salts from Sigma Aldrich, ACS reagent, 99% purity) to obtain a barium
178 loading of 16 wt.%. After drying at 100 °C for 12 h and calcination at 500 °C for 5 h (2 °C·min⁻¹
179 heating ramp) a Ba-Ru/SiO₂ DFM is finally obtained.

180 A similar preparation method has been used, reversing the order of impregnation: at first, Ba is dry
181 impregnated on SiO₂ (16 wt% load, Barium acetate precursor). After drying (100 °C, 12 h) and
182 calcination (500 °C, 5 h, 2 °C·min⁻¹ heating rate), the so-obtained Ba/SiO₂ sample has been dry
183 impregnated with ruthenium nitrosyl nitrate (0.5 wt%) and finally just dried at 120 °C overnight to
184 obtain a Ru-Ba/SiO₂ DFM. This last procedure has been performed also to prepare a DFM with
185 increased Ba loading (32 wt.%), namely Ru-32Ba/SiO₂. Synthesis procedures have been chosen
186 according to results previously published [22,25].

187 The list of prepared catalysts together with their composition is reported in Table 1. The nominal
188 content of Ru and Ba was confirmed through EDX analysis (Table S1).

189

190 *2.2. Catalysts characterization*

191 The prepared catalysts have been characterized in terms of morphology, chemico-physical properties,
192 and catalytic activity in CO₂ methanation.

193 Brunauer-Emmett-Teller (BET) analysis was performed by adsorption-desorption of nitrogen at -196
194 °C using a Micrometrics Tristar 300 instrument. Prior to the measurement all samples were outgassed
195 under vacuum at 120 °C for 3 h. Specific surface areas and adsorption-desorption isotherms
196 calculated by Brunauer-Emmett-Teller (BET), and Barret-Joyner-Halenda (BJH) method,
197 respectively from the adsorption and desorption branch of the isotherm data.

198 X-Ray diffraction (XRD) patterns were collected using a Panalytical diffractometer (Empyrean
199 model) in Bragg-Brentano geometry fitted with a copper tube (Cu K α radiation). The data sets were
200 acquired in continuous scanning mode over the 2 θ range 5 – 70 °, using a step interval of 0.0260 °
201 and step time of 110 seconds. Inorganic Crystalline Structure Database (ICDS) has been used to
202 recognize the crystalline phases.

203 Skeletal Fourier Transform Infrared Spectroscopy (FT-IR) spectra of catalyst powders have been
204 recorded in a Nexus FT-Instrument (ThermoNicolet) equipped with a ATR accessory (diamond
205 window), collecting 100 scans with a resolution of 4 cm⁻¹ and background air (DTGS detector and
206 OMNIC software).

207 H₂-TPR has been performed using a TPDRO 1100 instrument (ThermoFisher) to assess the
208 reducibility of the fresh materials by feeding 5% H₂/Ar from room temperature to 500 °C (heating at
209 10 °C/min). Ru dispersion was obtained through H₂ chemisorption using the same equipment,
210 performed through pulsing 5% H₂/Ar at 100 °C on the reduced samples. The values of Ru dispersion
211 and particle dimension have been calculated using correlations provided by Bergeret et al. [39], which
212 have been reported in the supplementary material. The reduced samples are then passivated in O₂ (2%
213 O₂, 1h at room temperature) and characterized with the previously mentioned techniques.

214 Adsorption and desorption experiments have been carried out in transmission mode over pure powder
215 disks (25 mg average disks weight) directly in the IR cell connected to a conventional gas
216 manipulation apparatus. For these experiments as well as CO₂-TPD, H₂-TPSR and H₂-CO₂ cofeeding
217 tests, described in the following, the same FT-IR instrument was used (DTGS detector, 100 scans,
218 4 cm⁻¹ resolution and OMNIC software). Before any adsorption experiment, samples were activated
219 in vacuum (10⁻³ Torr) for 1h at 500 °C or reduced at the same temperature in hydrogen and
220 subsequently outgassed at 500 °C (Ru/Ba sample). PY adsorption was performed at room temperature
221 over the activated samples and spectra of the surface species were recorded at each desorption step
222 in the range 150-400 °C. CO adsorption has been carried out employing a specific quartz cell with an
223 external chamber for liquid nitrogen with a thermocouple located in a specific position near the self-
224 supported disk sample. Tests were performed at liquid nitrogen temperature and spectra were
225 recorded upon outgassing at increasing temperature by progressive removal of liquid nitrogen from
226 -140 °C to room temperature or higher.

227 FT-IR CO₂ adsorption and desorption in programmed temperature (CO₂-TPD) experiments were
228 performed by introducing into the IR cell 18 Torr of pure CO₂ at room temperature and following
229 outgassing at R.T. during 1h. Subsequently, spectra of the surface species were recorded at each
230 desorption T-step in the range 150-500 °C.

231 FT-IR H₂ temperature programmed surface reduction (H₂-TPSR) tests were carried out by employing
232 the same instrument and conditions described above. After CO₂ adsorption phase and outgassing at
233 room temperature, 140 Torr of pure hydrogen were introduced in the IR cell at room temperature,
234 and then spectra of the surface species and gas phase were recorded at each temperature in the range
235 150-500 °C maintaining H₂-atmosphere. The CO₂ capture step was carried out at low temperature
236 [40,41] due to the thermodynamic advantage of adsorption under these conditions.

237 In another set of experiments, FT-IR CO₂-H₂ cofeeding experiment were performed. A mixture of
238 CO₂/H₂ (excess H₂) was added in the IR cell on the pre-reduced Silica-based sample. Spectra of gas-

239 phase species and spectra of surface species were recorded at 200, 250, 300, 350 and 400 °C and after
240 outgassing at room temperature following reaction.

241

242 2.3. Catalytic activity

243 Catalytic testing was performed loading 60 mg of sieved catalyst (75-106 μm particle diameter) in
244 packed bed quartz microreactors (7 mm internal diameter).

245 Temperature was monitored and controlled by using a K-type thermocouple positioned in the center
246 of the catalytic bed. The composition of the gas phase exiting the reactor was continuously analyzed
247 with a mass spectrometer (Pfeiffer Vacuum QMS200 quadrupole, analysis every 4s) and a micro gas
248 chromatograph (Agilent 3000, analysis every 180s).

249 The inlet flowrate of the experiments was set to $100 \text{ mL(STP)} \cdot \text{min}^{-1}$, resulting in a space velocity of
250 $100 \text{ L(STP)} \cdot \text{h}^{-1} \cdot \text{g}_{\text{DFM}}^{-1}$. The flowrate was kept constant also when introducing reagent gases in the
251 reactor (i.e. CO_2 , H_2) by using two six-way valves, allowing to obtain a precise pulse when switching
252 gases.

253 Different experiments have been performed to evaluate the catalytic performances of the catalysts:
254 CO_2 Temperature Programmed Desorption (CO_2 -TPD) and Temperature Programmed Surface
255 Reaction (H_2 -TPSR). Before each experiment, the catalyst was pretreated under H_2 atmosphere (4%
256 v/v in He) at 500 °C (heating rate of $10 \text{ }^\circ\text{C} \cdot \text{min}^{-1}$) to remove eventual adsorbed species.

257 CO_2 -TPD tests were carried out after the samples were saturated with CO_2 by feeding a stream
258 containing CO_2 (1% v/v in He) at 150 °C for 15 minutes. Eventually, the CO_2 flow was switched off
259 and the temperature was increased to 500 °C in He (heating rate of $10 \text{ }^\circ\text{C} \cdot \text{min}^{-1}$). In the H_2 -TPSR
260 experiment, after CO_2 adsorption (in the same conditions as CO_2 -TPD), H_2 (4% v/v in He) has been
261 fed to the reactor, and the temperature was increased to 500 °C in He (heating rate of $10 \text{ }^\circ\text{C} \cdot \text{min}^{-1}$).

262 The quantitative evaluation of the evolved species was determined by integrating the concentration
263 profiles over time during the TPD and TPSR tests, as described by Eq. 1:

$$\left[\frac{\mu\text{mol}_i}{\text{g}_{\text{DFM}}} \right] = \int C_i dt \cdot \frac{Q}{22.414} \cdot \frac{1}{\text{g}_{\text{DFM}}} \quad \text{Eq. 1}$$

264 where g_{DFM} refers to the amount of fresh DFM-sample loaded in the reactor, C_i is the concentration
 265 of i -species ($i = \text{CO}_2, \text{CO}, \text{CH}_4$) measured during each run (ppm), t is the time (s) and Q is the total
 266 volumetric flow rate ($\text{mL} \cdot \text{min}^{-1}$) measured at standard temperature and pressure conditions (298 K
 267 and 1 atm).

268

269 3. Results and discussion

270 3.1. Catalyst Characterization

271 ***N₂ adsorption – desorption analysis*** - Isotherms are reported in Figure 1. Bare SiO_2 and DFMs exhibit
 272 type IV physisorption isotherms and type H3 hysteresis loops [42]; moreover, the pore size
 273 distribution reveals a single main peak for all the catalysts.

274 As reported in Table 1, the surface area of the bare silica decreased considerably upon Ba addition,
 275 whereas the effect of Ru incorporation was negligible, as also observed in the literature [43].

276 Moving from binary catalyst (i.e Ru/SiO_2) to DFM one (i.e $\text{Ba-Ru}/\text{SiO}_2$), whatever the impregnation
 277 order is, it is possible to observe a reduction in both surface area and pore volume, in line with
 278 literature results on similar ternary catalysts [22], while the average pore diameter remained between
 279 11.3 and 14.7 nm. Notably, when the first impregnation step is with barium, the decrease in the surface
 280 area is greater (128 versus $180 \text{ m}^2 \cdot \text{g}_{\text{cat}}^{-1}$), possibly due to the direct incorporation of Ba species into
 281 the silica pores, as evidenced by the slight decrease in pore volume. This results more evident at
 282 higher Ba loading (e.g. 32% w/w).

283

284 **Table 1.** Nominal metal content, morphological characterization results of prepared DFMs.

Sample	Ru-loading (wt.%)	Ba-loading (wt.%)	S_{BET} ($m^2 \cdot g_{DFM}^{-1}$)	V_P ($cm^3 \cdot g_{DFM}^{-1}$)	$d_{p,avg}$ (nm)
SiO ₂	0	0	360	0.83	8.8
16Ba/SiO ₂	0	16	212	0.60	10.8
0.5Ru/SiO ₂	0.5	0	353	0.81	8.9
16Ba-Ru/SiO ₂	0.5	16	180	0.52	11.3
Ru-16Ba/SiO ₂	0.5	16	128	0.47	14.7
Ru-32Ba/SiO ₂	0.5	32	87	0.29	13.7

285

286 **X-ray diffraction** - XRD patterns recorded for commercial silica and all the bimetallic DFMs are
 287 reported in Figure 2. The monometallic samples, 16Ba/SiO₂ and Ru/SiO₂, exhibited only slight
 288 modifications compared to the typical amorphous silica pattern of the support. In particular,
 289 16Ba/SiO₂ displayed diffraction reflexes corresponding to the orthorhombic phase of BaCO₃
 290 (witherite, JCPDS No. 5-378) at 23.9 °, 24.2 °, 34.6 °, 41.9 °, and 44.8 °. These peaks increased in
 291 intensity over time when the samples were aged under ambient conditions, a phenomenon already
 292 reported in the literature [25,44].

293 Ru/SiO₂ sample exhibited very weak diffraction lines at 28.1 °, 35.1 °, 40.0 °, and 54.3 ° attributable
 294 to RuO₂ tetragonal phase (JCPDS No. 43-1027); the very low intensity could be due to the tiny
 295 amount of metal (i.e. 0.5% wt.) and/or to the small RuO_x crystallite size.

296 In all the bimetallic samples, containing both Ba and Ru (Figure 2d-f, and S1), the XRD patterns were
 297 similar, showing pronounced peaks corresponding to BaCO₃ witherite-phase. The XRD pattern
 298 reported in the literature for an analogous 16Ba-Ru sample supported on γ -Al₂O₃ agrees with our
 299 results indicating that carbonate species are predominant [25]. It should be noted that the diffraction
 300 features related to the RuO₂ phase are largely masked by the intense Ba-carbonate peaks, with only
 301 the diffraction at 40.0 ° and 54.3 ° detectable, although very weak, due to the low Ru concentration in
 302 these samples.

303 **IR characterization** - Figure 3 reports the ATR - IR skeletal spectra of prepared DFMs where all the
304 spectra intensities are normalized to the Si-O structural main band. The spectra show typical peaks
305 around 1050 cm^{-1} (broad), 800 cm^{-1} and 460 cm^{-1} , due to the IR-active vibrational fundamental modes
306 of silica related to the asymmetric stretching and symmetric stretching and bending modes of Si-O-
307 Si bonds organized in SiO_4 tetrahedron (Figure 3, spectrum a) [45]. These features are similar in the
308 spectra of all silica-supported samples, regardless of the preparation procedure.

309 The pronounced shoulder detected between $980\text{-}950\text{ cm}^{-1}$ has been reported to be due to the Si-OH
310 vibrational mode and sensitive to surface modifications [46]. Its significant intensity is consistent
311 with the presence of exposed silanol groups still detectable after the incorporation of Ba and Ru
312 promoters. Indeed, these cations do not enter significantly the bulk structure due to the preparation
313 method chosen and to the mild calcination temperature (i.e. $500\text{ }^\circ\text{C}$).

314 After Ba addition (Figure 3, spectrum c), several new bands in the region $1500\text{-}600\text{ cm}^{-1}$ are detected,
315 namely at 1430 , 856 and 693 cm^{-1} , typical of presence bulk carbonate ions [47]. As reported also for
316 other materials [48] this suggests that the presence of these cations at the surface is associated with
317 that of corresponding oxide ions, which are characterized by surface high basicity. This leads to the
318 formation of carbonate ions by adsorption of CO_2 from the environment and/or after calcination of
319 the acetate Ba precursor.

320 These features are common to all samples, regardless of the order of impregnation of Ba and Ru
321 (compare Figure 3, spectra d and e). Moreover, when the barium loading was increased (Figure 3,
322 spectrum f), the $[\text{BaCO}_3\text{-bulk}]:[\text{Si-O-Si}]$ intensity ratio correlated well with the higher loading of the
323 storage element, being 3.5 times greater than that calculated for samples containing 16 wt.% Ba.
324 Thus, an increased promoter loading preferentially leads to the formation of bulk-type BaCO_3 species
325 upon calcination, while the impregnation order did not influence the surface density of these species.
326 To complete the superficial characterization, the OH stretching region has been analyzed by FT-IR
327 after outgassing at $500\text{ }^\circ\text{C}$ for 1h and the results are reported in Figure 4.

328 Silica spectrum is consistent with literature reports, showing the cut off at 1300 cm^{-1} , typical of silica-
329 based materials, overtones of bulk vibrations in the region $2100\text{-}1500\text{ cm}^{-1}$ and the sharp band of the
330 OH stretching mode of free-surface silanols at 3745 cm^{-1} [49] (see Figure S1). The latter band is
331 reduced in intensity in the spectrum of the Ba-containing samples and appears more complex. The
332 addition of Ru does not introduce significant modifications in the silica OH groups, likely due to the
333 very low amount of the metal, while a further reduction in intensity of this band is observed in the
334 spectrum of the sample at the highest Ba loading (Figure 4, spectrum f). This observation provides
335 evidence of the perturbation of the surface by oxide species, which limits the amount of exposed
336 silanols and induces some heterogeneity of the surface hydroxyls. Apparently, the sequence of the
337 impregnation procedure does not affect the surface properties of this system. As discussed in the
338 previous section, bands due to surface and bulk carbonate species are detected in the low frequency
339 region ($1600\text{-}1300\text{ cm}^{-1}$) in the samples containing Ba oxides, clearly indicating the basic character
340 of this surface (see Figure S1).

341

342 **Reducibility characterization** - Information on the reducibility of the catalytic samples was obtained
343 through H_2 -TPR experiments, as reported in Figure S2. 16Ba-Ru/SiO_2 (Fig. S2 a) shows the onset of
344 reduction at $185\text{ }^\circ\text{C}$, with a main reduction peak centered at $260\text{ }^\circ\text{C}$ likely associated with the reduction
345 of residual barium carbonates formed during calcination. This interpretation is supported by the XRD
346 pattern of the reduced and passivated 16Ba-Ru/SiO_2 sample (Fig. S3), which differs significantly
347 from the fresh material (Figure 2): the disappearance of the crystalline BaCO_3 reflections indicates
348 its transformation into amorphous compounds (i.e., BaO), along with the presence of crystalline Ru^0 .
349 Results of N_2 physisorption carried out on the reduced 16Ba-Ru/SiO_2 sample show an increased BET
350 surface area compared to the fresh material (reduced: $220\text{ m}^2\cdot\text{g}_{\text{DFM}}^{-1}$ vs fresh: $180\text{ m}^2\cdot\text{g}_{\text{DFM}}^{-1}$), consistent
351 with the decomposition of the BaCO_3 phase. No significant changes in the shape of the physisorption
352 isotherm and pore size distribution are observed on the reduced sample (Figure S4).

353 In contrast, Ru-16Ba/SiO₂ sample (Fig. S2 b) begins to reduce at lower temperature (125 °C) and
354 presents a higher H₂ consumption compared to the previous material. This increased H₂ consumption
355 is attributed to the first thermal treatment carried out in the presence of both Ru and Ba, consistent
356 with the catalytic decomposition of the storage element by Ru [15]. In this case, three distinct
357 reduction peaks are observed and can be tentatively assigned to the reduction of Ru (210 °C), residual
358 Ba nitrates (360 °C) and Ba carbonates (450 °C). The continued H₂ consumption after holding the
359 temperature at 500 °C suggests that the reduction of BaCO₃ remains incomplete following the
360 activation procedure, leaving residual crystalline BaCO₃ (Figure S3). The presence of crystalline
361 BaCO₃ after reduction is reflected in the BET surface area, which remains essentially identical to that
362 of the fresh material (reduced: 127 m²·g_{DFM}⁻¹ vs fresh: 128 m²·g_{DFM}⁻¹). As in the previous case, no
363 significant changes in the shape of the physisorption isotherm and pore size distribution are observed
364 (Figure S4).

365 The same three peaks of H₂ consumption observed with Ru-16Ba/SiO₂ are present also with Ru-
366 32Ba/SiO₂, although the peaks associated with Ru reduction and carbonate reduction appear more
367 intense and are shifted to higher temperatures (respectively, 280 °C and 480 °C). This behavior is
368 expected due to the higher Ba loading in the material.

369 The dispersion of Ru was determined by H₂ chemisorption pulse experiment for 16Ba-Ru/SiO₂, Ru-
370 16Ba/SiO₂ and Ru-32Ba/SiO₂ samples and included in Table S1, along with the corresponding
371 calculated average Ru particle dimension. The lower Ru dispersion observed for 16Ba-Ru/SiO₂
372 compared to Ru-16Ba/SiO₂ might be attributed to the calcination procedure applied on the former
373 after the Ru impregnation step.

374

375 **Acidity characterization** - The acidity properties of the catalytic surface have been investigated by
376 FT-IR spectroscopy using pyridine as probe molecule. The resulting spectra after outgassing at 150

377 °C are reported in Figure 5 for bare SiO₂, Ru/SiO₂ and Ru-16Ba/SiO₂ as exemplification of different
378 formulations.

379 Silica is a weak protonic acid, so adsorption of pyridine and its following desorption at 150 °C gives
380 rise to weakly adsorbed species, characterized by IR bands at 1597 and 1446 cm⁻¹ due to H-bonded
381 pyridine molecules interacting with surface silanols. Correspondingly, stretching bands of isolated
382 OH groups appear as negative features in the subtraction spectra, giving rise to a broad absorption
383 centered near 3500 cm⁻¹ (see also Figure S5).

384 The modification with Ba ions increases the basicity of the surface, and also appears to add Lewis
385 acidity, as revealed by the weak band at 1617 cm⁻¹ due to pyridine molecules coordinated over
386 medium strength Lewis sites (Figure 5, spectra b and c) [50,51]. Also in this spectrum, silanol groups
387 still exposed at the surface allow interaction through H bonds, as revealed by the negative band in the
388 high frequency region of the IR spectrum (see Figure S5). In parallel, bands due to H-bonded pyridine
389 appear at 1596 cm⁻¹. The same conclusions apply to the surface of the Ru-containing catalyst (Figure
390 5, spectrum c), where some Lewis acidity can be related to the Ru ions, although in negligible amount
391 due to the very low loading of the metal.

392

393 ***CO adsorption and FT-IR characterization*** - CO adsorption at low temperatures has also been
394 carried out over the SiO₂ and Ba/SiO₂ samples. The spectrum of CO adsorbed over silica (see Figure
395 S6 a) shows a main sharp band at 2156 cm⁻¹ (CO stretching region), due to CO weakly interacting
396 with the support through H-bonds, together with a pronounced shoulder at ~2139 cm⁻¹, due to the
397 presence of liquid-like CO. Outgassing at increasing temperature (from -140 °C to 150 °C) results in
398 the rapid disappearance of both components, according to their weak interaction with the surface. The
399 main features described above are present also in the spectra of CO adsorbed over the Ba-containing
400 silica (Figure S6 b); however, after outgassing, the wavenumber of the former components shifts to
401 higher values (from 2157 to 2168 cm⁻¹), according to the behavior of CO adsorbed over metal oxides

402 ions. These results are in good agreement with those of pyridine adsorption, confirming that metal
403 ions generate Lewis sites exposed at the surface.

404 Low temperature CO adsorption has also been carried out over the reduced Ru-16Ba/SiO₂ sample
405 and the corresponding spectrum is shown in Figure 6. Starting from -140 °C a very complex pattern
406 of IR features due to carbonyl species is detected. The main band centered at 2155 cm⁻¹ and quickly
407 disappearing following outgassing is related to CO interacting with the hydroxyl groups of silica. A
408 broad band centered at 2053 cm⁻¹ with shoulders near 2000 cm⁻¹ and 2100 cm⁻¹ is observed, assigned
409 to (multi)carbonyl species [Ruⁿ⁺(CO)₂₋₄], having a partially oxidized character, and to linearly
410 adsorbed CO on Ru⁰ species, likely isolated and defective sites. Another weak component at 2137
411 cm⁻¹, together with a shoulder near 2090 cm⁻¹, can also characterize carbonyls coordinated on partially
412 oxidized Ru and on Ru ions [52].

413 By increasing the temperature, i.e. by lowering the CO coverage, the high frequency components are
414 almost completely lost, and the 2053 cm⁻¹ band broadened and shifted to lower frequencies. At 100
415 °C, a broad absorption is still detectable, centered at 2038 cm⁻¹ together with a further broad shoulder
416 extending in the 2000-1950 cm⁻¹ region and likely associated with bridging species. This band shifting
417 upon outgassing is due to carbonyls adsorbed on extended Ru metal particles, whose frequency
418 decreases at low CO coverage due to the well-known coupling effects [52].

419 These data indicates that even after reduction in hydrogen cationic Ru species can be detected, likely
420 interacting with the support. At the same time, small amounts of isolated or clustered Ru metal
421 particles (bands in the 2100-2000 cm⁻¹ range) and large metal particles (2060-2030 cm⁻¹) are also
422 observed.

423

424 **Co-feeding CO₂/H₂** - The co-feeding of CO₂ and hydrogen has been directly carried out in the IR cell
425 at high temperatures, in order to study the state of active Ruthenium in an atmosphere mimicking the
426 methanation reaction. The results obtained over Ru-16Ba/SiO₂ catalyst are reported in Figure 7. In

427 these conditions, the formation of gaseous CH₄ together with CO traces has been detected in the IR
428 cell in the temperature range from 250 °C to 400 °C (Figure 7A), showing the capability of this
429 catalytic system to perform a non-selective CO₂ reduction. IR Spectra of the surface species shows a
430 sharp band at 2345 cm⁻¹ due to linearly adsorbed CO₂ (OCO asymmetric stretching) decreasing in
431 intensity during the reaction. A mixture of bicarbonate and carbonate species (bands at 1650, 1588,
432 1452 and 1391 cm⁻¹) formed and coordinated on barium centers, whose intensity increases at
433 increasing temperature, is also detectable. The peak at 1622 cm⁻¹ is due to vibrational mode of
434 adsorbed water, increasing in intensity as a product of methanation reaction in the IR cell.

435 As soon as CO is formed, i.e. between 200 °C and 250 °C, the main feature in the IR spectrum is a
436 broad and complex band centered at 2030 cm⁻¹, with shoulders at 2000 cm⁻¹ and possibly 2045 cm⁻¹
437 (Figure 7B and magnification) characterizing strongly adsorbed CO species. A broad and weak
438 absorption at about 1895 cm⁻¹ is overlapping with overtone features of the silica support.

439 The 2030 cm⁻¹ band (LF band) has been typically assigned by several authors to carbonyl species
440 linearly coordinated over reduced, metallic Ru particles, in agreement with the band position
441 characteristic of CO adsorption on Ru single crystals [53]. The complexity of the band suggests the
442 presence of several Ru species exposed at the surface and revealed already at such low CO coverage.
443 Namely, the presence of the poorly resolved shoulders at frequencies higher than 2050 cm⁻¹ could be
444 due to (multi)carbonyl species on Ru having a partially oxidized character [54] and to linearly
445 adsorbed CO on high energy defects sites and isolated Ru⁰ species surrounded by partially oxidized
446 Ru [55]. The component below 2000 cm⁻¹ has been associated with another, more labile, on-top
447 carbonyl species [52]. In the temperature range 250-350 °C, CO and methane formation are increasing
448 in the gas phase (Figure 7A) and consequently, the carbonyl coverage increases at the surface [56].
449 Features of carbonyl species become sharper and stronger, and apparently low frequency components
450 are almost lost. Possibly, a shoulder near 2070 cm⁻¹ grows and can be evidenced in the magnification
451 spectrum (Figure 7B). Such a high frequency component could be related again to carbonyls

452 coordinated over partially oxidized Ru [55]. The predominance of the LF band on the other features,
453 identified as carbonyl species on partially oxidized Ru, is a consequence of the differences in the
454 dispersion of the metal phase. As a matter of fact, the appearance of several CO adsorption bands in
455 the 2100-2000 cm^{-1} spectra region has always been related to metal particle size. For instance, the
456 presence of three CO bands has been reported when CO was adsorbed on finely dispersed Ru-alumina
457 samples with particle size less than 60 Å, but for CO adsorption on a sample with particle size greater
458 than 90 Å, only one band was seen [57]. Bands of adsorbed water are detected at 1622 cm^{-1}
459 (deformation mode of H_2O [58]) and in the range 3200-3600 cm^{-1} (spectral region not shown). In this
460 spectral region several components can be highlighted: at 3630, 3550 and 3050 cm^{-1} due to stretching
461 modes of OH groups of the silica support involved in H-bonds and to adsorbed water. Finally, the
462 decrease in intensity of the bridging band in favor of the linear carbonyl species is also completely
463 consistent with the increasing CO coverage. It is interesting to note that no HF bands can be detected
464 above 2100 cm^{-1} diagnostic of $\text{Ru}^{n+}(\text{CO})_{2-4}$ species, suggesting that CO induced oxidation of Ru does
465 not occur on the silica barium catalyst, even at such high temperature [59].

466 Summarizing, conditioning the catalyst surface in these experimental conditions, i.e. a strongly
467 reducing environment and high temperatures, results in a low dispersion of supported ruthenium
468 particles, which become smoother (less defective) than those detected following hydrogen reduction
469 of the sample. resent of an electron-donating effect from the basic O^{2-} species of the Ba oxide. Also,
470 the presence of water vapor arising from methanation of CO_2 can cause agglomeration of the Ru
471 particles (see the growing of methane diagnostic band at 3015 cm^{-1} in the gas phase spectra [58].

472

473 3.2. DFMs methanation activity

474 The catalytic activity of DFMs has been evaluated by means of microreactor experiments combined
475 with FT-IR spectroscopy in order to elucidate the superficial features that could justify the observed
476 behaviors. Note that only the sample containing both Ru and Ba exhibit CO_2 desorption capacity.

477

478 *3.2.1. CO₂ temperature programmed desorption (CO₂-TPD)*

479 CO₂-TPD experiments have been carried out over all the ternary DFMs. Figure 8 shows the evolution
480 of the CO₂ concentration profile as a function of temperature up to 500 °C after CO₂ adsorption; the
481 corresponding amounts of desorbed CO₂ are reported in Table 2.

482 In general, it is possible to identify three distinct desorption regions: a low-temperature region (150-280
483 °C), a medium-temperature region (up to 350 °C), and a high-temperature region (up to 500 °C). This
484 suggests the presence of distinct carbonate species with varying thermal stability and strength, with
485 the low- and medium-strength species being the predominant carbonate population, while the species
486 that remained adsorbed at temperatures above 350 °C were less abundant.

487 In all cases, the CO₂ desorption profile exhibited a broad desorption peak with a maximum between
488 200 °C and 230 °C, showing a decreasing desorption trend with increasing temperature. After reaching
489 500 °C, almost all the adsorbed species are decomposed (C-balance close within 10%). Note that the
490 impregnation of barium at first lowered the CO₂ desorption maximum (compare curve a and b),
491 suggesting that a higher amount of weak basic sites are present on the Ru-16Ba/SiO₂ than on the
492 16Ba-Ru/SiO₂ sample (see FT-IR results discussed below).

493 When the barium loading increases (from 16% to 32% wt, Figure 8, curve c), the CO₂ desorption
494 profile becomes more complex, suggesting a different array of carbonate species. Indeed, thermal
495 desorption occurs mainly between 200 °C and 450 °C and the amount of CO₂ released stays steady
496 up to 500 °C, indicating that higher temperatures are needed to completely desorb the carbonates, so
497 the sample mainly has medium to strong basic properties.

498 As reported in Table 2, the amount of CO₂ desorbed (used as a measure of the storage capacity) is 42
499 $\mu\text{molCO}_2 \cdot \text{g}_{\text{cat}}^{-1}$. Furthermore, by increasing the Ba loading, the desorbed CO₂ increases as well. Note
500 that the impregnation order does not seem to affect the CO₂ storage capacity.

501

502

Table 2. CO₂ adsorption capacity of DFMs samples

Sample	CO ₂ ^{desorbed} -TPD ($\mu\text{mol}\cdot\text{g}_{\text{DFM}}^{-1}$)	CH ₄ ^{produced} -TPSR ($\mu\text{mol}\cdot\text{g}_{\text{cDFM}}^{-1}$)	CO ₂ ^{produced} -TPSR ($\mu\text{mol}\cdot\text{g}_{\text{DFM}}^{-1}$)
16Ba-Ru/SiO ₂	42	37	0
Ru-16Ba/SiO ₂	41	34	0
Ru-32Ba/SiO ₂	56	53	11

503

504 The nature and thermal stability of the species formed upon CO₂ adsorption were studied for the SiO₂-
 505 based samples using FT-IR spectroscopy. To ensure maximum adsorption, the samples activated in
 506 vacuum were saturated with CO₂ at room temperature before being subjected to outgassing with
 507 increasing temperatures from 150 °C to 500 °C. The resulting subtracted spectra are presented in
 508 Figure 9 in the region above the cut-off of silica support. Note that 16Ba-Ru/Al₂O₃ has been reported
 509 also for comparison purposes.

510 CO₂ adsorption-desorption FT-IR test performed on 16Ba/SiO₂ (Figure S7) already shows the
 511 formation of a complex system of species, summarized in Figure 10, within the carbonate region
 512 (1800-1320 cm⁻¹). A band at 1690 cm⁻¹ is attributed to the initial formation of weakly adsorbed
 513 bicarbonate species associated with interactions with hydroxyl groups of basic element, likely present
 514 at the catalyst surface [47], and disappeared after mild outgassing. Bands centered at 1650, 1620,
 515 1462, and 1378 cm⁻¹ were detected and assigned to various surface carbonate species of the bidentate
 516 chelate type [47,60,61] formed on the Ba oxide.

517 Similar signals were observed in the case of Ru-Ba-containing catalysts. For the 16Ba-Ru/SiO₂
 518 sample, i.e. Ru impregnated first (Figure 9A), exposure to CO₂ at room temperature resulted in the
 519 formation of a complex system of species within the carbonate region. A band at 1690 cm⁻¹, is
 520 attributed to the initial formation of weakly adsorbed bicarbonate species associated with interactions
 521 with hydroxyl groups of basic dopant and oxides on silica [47] disappearing after mild outgassing.
 522 Bands centered at 1650, 1620, 1495, and 1378 cm⁻¹ were detected and assigned to various surface

523 carbonate species of the bidentate chelate type [50,61,62] formed on the Ba oxide. The band at
524 1378 and 1495 cm^{-1} , attributed to a strongly bonded bidentate chelate species, were observed upon
525 CO_2 exposure and subsequent quick degassing. Additionally, a shoulder at 1347 cm^{-1} , attributed to
526 weaker adsorbed monodentate surface carbonates [62], was also observed disappearing after
527 outgassing for one hour and was completely absent at higher temperatures. Although the intensities
528 of the 1650 and 1620 cm^{-1} bands decreased slightly by increasing temperature up to 150 $^\circ\text{C}$ were still
529 detectable while 1495 and 1380 cm^{-1} bands were maintained. As the temperature increased, chelating
530 bidentate carbonate-species features gradually diminished, and a new broad peak emerged at 1550
531 cm^{-1} , attributed to bridging bidentate carbonate species [25,47,48,62], suggesting an evolution from
532 bidentate chelating carbonates into bridging bidentate species with temperature still observable at 500
533 $^\circ\text{C}$.

534 In particular, analyzing the influence of the precursor impregnation order by first impregnating the
535 alkali(-earth) and subsequently the noble metal (i.e. Ru-16Ba/ SiO_2 , Figure 9B), a peak at 1495 cm^{-1}
536 was also observed upon CO_2 exposure and subsequent quick degassing. This band is attributed to a
537 strongly bonded bidentate chelate species possibly resulting from the interaction between Ba and Ru
538 oxide species. The peak at 1378 cm^{-1} can be assigned to an even stronger chelating bidentate
539 carbonate species related to BaO-phase close to Ru-atoms. Additionally, a shoulder at 1347 cm^{-1} ,
540 attributed to weaker adsorbed monodentate surface carbonates, was also observed [62,63]. After one
541 hour of outgassing and heating to 150 $^\circ\text{C}$, the 1690 cm^{-1} and 1347 cm^{-1} bands, weakly bonded
542 bicarbonate and monodentate carbonates respectively, disappeared, confirming the complete removal
543 of these species, the intensities of the 1650 and 1620 cm^{-1} bands slightly decreased, while the 1495
544 and 1380 cm^{-1} bands, corresponding to more strongly adsorbed bidentate chelated carbonates,
545 maintained their intensity. Also, the band at 1650 and 1620 cm^{-1} gradually diminished, and a new
546 broad peak emerged at 1550 cm^{-1} attributed to bridging bidentate carbonate species but not observable
547 at 500 $^\circ\text{C}$ suggesting when the Ba promoter is added onto Ru (Ba-Ru), the probability of the presence

548 of isolate BaO phase domains at the surface increases together with the formation capability of stable
549 carbonate species which require higher temperatures to desorb compared to Ru-Ba.

550 The modified stability of Ba carbonate species is expected to correlate with the preparation method.
551 Since the Ru precursor solution contains nitric acid, its impregnation over Ba/SiO₂ leads to the
552 chemical decomposition of Ba carbonates formed during calcination of the acetate precursor. As a
553 result, Ba nitrates are generated, which decompose more readily into BaO in presence of H₂ (i.e.
554 pretreatment conditions) compared to Ba carbonates [64]. Similar results were reported by Jeong-
555 Potter et al. [65] for Ru-Na₂O/Al₂O₃ DFM-samples. The authors confirmed that the sample
556 preparation method is inconsequential for Ru DFM systems. Ru in nitrate or oxide form can be
557 sufficiently reduced during in situ prereduction to methanation active Ru⁰, thereby catalytically
558 decomposing Na₂CO₃ to “Na₂O” and producing more active sites for CO₂ adsorption. Ru indirectly
559 contributes to the enhanced CO₂ adsorption capacity by facilitating the decomposition of the
560 precursor salts, liberating more adsorption sites.

561 Furthermore, after three cycles of CO₂ adsorption and TPD, the CO₂ uptake of Ba-Ru was found to
562 be completely inhibited (data not shown), resulting in a loss of storage capacity. This inhibition is
563 likely due to the increased stability of carbonates in this configuration, caused by the gradual build-
564 up of stable carbonate species. The lower regenerability of Ba-Ru is the main reason for adopting the
565 Ru-Ba impregnation procedure for the preparation of Ru-32Ba/SiO₂.

566
567 FT-IR spectra after CO₂ adsorption over Ru-32Ba/SiO₂ catalyst are reported in Figure 9C. Notably,
568 compared to its analogue with half the Ba concentration (Figure 9B), the spectral scale is doubled,
569 indicating a higher relative concentration of overall detected species, in line with the overall enhanced
570 CO₂ adsorption capacity (see Table 2). A pronounced formation of monodentate carbonate species,
571 centered at 1347 cm⁻¹, was observed, that persisted until 150 °C, in contrast to the sample containing
572 16 wt.% Ba. This effect is attributed to a higher surface population of Ba-oxide, which favors the

573 formation of such species. A shoulder at 1690 cm^{-1} , likely corresponding to bicarbonate species on
574 was also detected; these species were rapidly desorbed upon outgassing. Peaks at 1650, 1620, 1500,
575 and 1375 cm^{-1} were attributed to the formation of bidentate chelate carbonates. The weaker bonded
576 species (1650 and 1620 cm^{-1}) disappeared above $150\text{ }^{\circ}\text{C}$, evolving into bridging bidentate carbonates
577 (1550 cm^{-1}). This bridging carbonate signal remained more thermally stable and exhibited greater
578 intensity compared to the analogous Ru-16Ba/SiO₂ sample. The increased population of isolated and
579 proximal BaO sites appears to favor the formation of strongly adsorbed bridged bidentate carbonates,
580 which gradually desorb, as confirmed by CO₂-TPD tests in a microreactor (Figure 8c). On the
581 contrary, the formation of bidentate carbonates, associated with BaO in proximity to Ru sites (1500
582 and 1375 cm^{-1}), was suppressed, consistent with the increased Ba concentration. These species
583 desorbed and became undetectable above $150\text{ }^{\circ}\text{C}$. Overall, increase the Ba loading results in an
584 improved CO₂ adsorption capacity, mainly achieved through the formation of bidentate chelating
585 carbonates that evolve into bridging bidentate species, considerably more thermally stable (medium-
586 high strength adsorption).

587 This complex carbonate population could be described considering the superficial distribution of Ba
588 and Ru and their reciprocal proximity; a general scheme is reported in Figure 10. Chelating bidentate
589 carbonates (1650 and 1620 cm^{-1}) are likely primarily located on isolated or closely spaced barium
590 oxide sites on the catalyst surface (configuration I and II). These species could be weaker bonded
591 than those formed when Ba is close to Ru sites (configuration III). Strongly bonded bidentate chelate
592 species (1495 cm^{-1} band) result from the interaction between Ba and Ru oxide species (configuration
593 IV). Moreover, bidentate chelating carbonates can evolve into bridging bidentate species (1550 cm^{-1})
594 when they are formed on BaO-BaO centers (configuration II) desorbed gradually at higher
595 temperatures due to stronger bonding carbonate character. When chelating bidentate carbonates
596 species are formed on well-dispersed BaO phase (1495 and 1380 cm^{-1}), a gradually desorption can

597 be observed with temperature, as evidenced by a progressive decrease in their band intensity. Their
598 isolated nature on the catalyst surface prevented their conversion into bridged carbonates.

599 This FT-IR analysis permits to associate CO₂ desorption peaks observed in during TPD with
600 superficial species of different nature: the stronger bidentate chelated carbonate species desorb
601 progressively with temperature as medium-strength adsorbed species, generating a CO₂ desorption
602 peak at temperature below 250 °C, whereas their evolution into bridging carbonate species
603 (configuration II in Figure 10), likely occurs only at temperatures higher than 300 °C.

604 The CO₂ storage capacity of the SiO₂-based catalysts results significantly lower than that of analogous
605 systems based on commercial γ -Al₂O₃ as support [22,25]. In comparison with the silica-supported
606 sample, a larger number of different and strong bands were observed following CO₂ adsorption
607 (Figure 9D). Indeed, exposed alumina support actively contributes to CO₂ adsorption in the form of
608 surface carbonates and hydrogen carbonates [22,66]. Namely, under CO₂ atmosphere and after
609 outgassing, a diagnostic peak at 1225 cm⁻¹, attributed to the formation of weakly adsorbed bicarbonate
610 species on the alumina support [52,67,68], was observed. These species disappeared after prolonged
611 outgassing. Also bands at 1650 and 1620 cm⁻¹, associated with the formation of bidentate chelated
612 carbonate species, progressively decreased during outgassing at room temperature, disappearing
613 above 200 °C, while a component at 1378 cm⁻¹, again attributed to strongly adsorbed bidentate
614 chelated carbonates, persisted with increasing temperature up to 500 °C band at 1555 cm⁻¹ was also
615 observed, becoming the predominant signal after outgassing at increasing temperatures, albeit with a
616 reduction in intensity from 300 °C onward, in parallel with a similar band detected over Silica-based
617 catalysts. This feature could be attributed to the preferential formation of bridging bidentate
618 carbonates likely involving Ba and Ru ionic species.

619 As a matter of fact, when using this Al₂O₃ as a support, the concentration of Ba and Ru atoms per m²
620 is 1.8 times higher than on Silica and this substantially increases the probability of forming highly
621 thermally stable carbonate-type species on close proximity BaO particles, [BaO-BaO]-CO₃. In sum,

622 the thermal stability of predominantly bridged bidentate carbonates (the major population) is higher
623 when alumina is employed; these species require higher temperatures for desorption. On the other
624 side, the use of silica favors the formation of chelated bidentate carbonates, which are less thermally
625 stable and evolve into bridging species that remain adsorbed until higher temperatures are reached.

626

627 3.2.2. *Temperature programmed surface reduction with hydrogen (H₂-TPSR)*

628 As in the case of CO₂-TPD, H₂-TPSR experiments were conducted by combining gas phase analysis
629 from microreactor system with FT-IR spectroscopy. The results of the former are reported in Figure
630 11.

631 On 16Ba-Ru/SiO₂ (Figure 11A) the adsorbed CO₂ reacts with H₂ to CH₄, that is observed with two
632 maxima at 231 °C and ~420 °C. The CH₄ concentration profile agrees with the presence on the surface
633 of a variety of carbonate species with different stability, as confirmed by the FT-IR CO₂-TPD, and
634 different reactivity towards H₂.

635 Note that the CH₄ peak is observed in correspondence of that of CO₂ released during TPD. Ru-
636 16Ba/SiO₂ catalyst also results active and selective in the methanation reaction (Figure 11B), although
637 in this case the methane production is moved at a higher temperature (266 °C). This shift could be
638 likely due to the lower reducibility of these carbonates requiring higher temperature to be converted
639 into methane. In both 16Ba-Ru and Ru-16Ba samples, any other product is observed, neither CO₂ nor
640 CO, suggesting a high selectivity for the methanation reaction on this system. Moreover, considering
641 the amount of CH₄ produced reported in Table 2, it is clear that stored CO₂ is not completely converted
642 into methane. In the literature there are indications on the lower performances of SiO₂-based catalysts
643 with respect to other support (e.g. Al₂O₃, TiO₂, CeO₂...), being the apparent activation energies of
644 CO₂ hydrogenation reaction depend on the nature of the support [69]. However, it should be noted
645 that the same selectivity was observed by Porta et al. [22,25,66] on Ru-Ba/Al₂O₃ DFMs. Moreover,
646 these authors observed the release of CO₂ before the methane production while it is absent in our

647 SiO₂-based catalysts. It could be suggested that on Al₂O₃-supported DFMs CO₂ is adsorbed onto the
648 support as well as on the Ba sites, forming more labile bicarbonate species that desorb at low
649 temperature without reaction with H₂. On the other hand, on SiO₂-supported DFMs the acidic nature
650 of the support inhibits the adsorption of CO₂ that occurs preferentially on Ba sites, resulting in more
651 stable carbonates that are reduced to CH₄ at lower temperatures than those on alumina-based material.
652 When the Ba loading is increased, a CO₂ desorption is still observed at 209 °C (as in the CO₂-TPD)
653 attributed to the cleavage of the weak bicarbonate bands while the CH₄ production starts at slightly
654 higher temperatures, reaching the maximum at 271 °C.

655 The initial incorporation of the storage element followed by the noble metal promotes a CO₂ capture
656 mechanism that selectively forms a higher population of medium-strength carbonates while
657 maintaining a CO₂ desorption capacity similar to that of the 16Ba-Ru/SiO₂ sample. This effect
658 resulted in a higher overall regeneration capacity at a lower temperature range and with quicker CH₄
659 generation, with a higher and more symmetric maximum peak. In contrast, when Ru is incorporated
660 after the storage element, a spillover effect is promoted, which is slower and favored at higher
661 temperatures upon H₂ introduction [25,70,71]. However, when the alkali (base) is introduced after
662 Ruthenium in catalysts supported on commercial silica, a portion of Ruthenium becomes blocked by
663 the presence of Ba. This reduces the *spillover* effect, thereby favoring a reduction of the generated
664 carbonates over a wider temperature range, as evidenced by the different CH₄ production temperature
665 ranges in the H₂-TPSR test.

666 The reducibility of the CO₂ adsorbed species was also investigated by FT-IR analysis for the 16Ba-
667 Ru/SiO₂ and Ru-16Ba/SiO₂ samples, the results are presented in Figure 12A and 13B, respectively.
668 In these experiments, the samples were saturated with CO₂ at room temperature to ensure maximum
669 adsorption and then subjected to prolonged outgassing at room temperature and subsequently to a
670 temperature ramp from 150 °C to 500 °C under a H₂ atmosphere. Note that only carbonates are
671 detected, whose intensity changes under H₂ flow. Potential reaction intermediates, such as Ru-

672 carbonyls or formate species, which have been reported for CO₂ methanation over Ru or Ni based
673 and Na or K based DFM catalysts supported over alumina(-ceria) [30,72–75], could not be clearly
674 identified probably because masked by the more intense carbonate bands and/or by the silica signals
675 in the spectral region of 1200-2050 cm⁻¹.

676 Consistent with the gas-phase results, a rapid and significant reduction of carbonate species was
677 observed in both samples when hydrogen was introduced as the temperature increased. However, the
678 distribution and evolution of the various carbonate species differed from the FT-IR results recorded
679 during CO₂-TPD (see Figure 10A and 11C).

680 In the case of 16Ba-Ru/SiO₂ sample, a marked reduction in the carbonate signals was observed after
681 introducing H₂ at room temperature and increasing the temperature to 150 °C (Figure 12A, curve b).
682 A complex absorption was detected, with a main maximum at 1624 cm⁻¹, which can be attributed to
683 low-strength bidentate chelated carbonate species as discussed before. Another component centered
684 at 1550 cm⁻¹ emerged at increasing temperature. This latter band corresponds to bridging bidentate
685 carbonate species formed via the early conversion of bidentate chelated species to bridging species
686 under reducing conditions at relatively low temperatures. With the increasing temperature to 250 °C,
687 the 1624 cm⁻¹ complex band gradually diminished in intensity and then increased again at higher
688 temperature. This behavior suggests that this band could be also associated with vibrational
689 deformation mode of adsorbed water (from the methanation reaction) at the catalyst surface as
690 reported by Kantcheva et al. [58]. A similar trend was observed for the 1550 cm⁻¹ band, which slightly
691 increased in intensity above 300 °C. In addition, the bands at 1495 and 1380 cm⁻¹, associated with
692 high-stability bidentate carbonate species, decreased in intensity by rising temperature. Both
693 bidentate chelated and bridging species show significant stability, with the bridging species
694 decomposing and reducing to CH₄ progressively as the temperature increases. Notably, the high-
695 strength bidentate species remain resistant even above 350 °C, gradually diminishing with further
696 temperature rise. It could be supposed that the weakly adsorbed carbonate species, identified as

697 monodentate and bidentate chelated species in the previous section, are rapidly converted to CH₄,
698 while medium-to-high strength carbonates (i.e. bridged bidentate) are likely reduced only at elevated
699 temperatures.

700 For the Ru-16Ba/SiO₂ sample (Figure 12B), a slightly different evolution of adsorbed species was
701 observed. Upon H₂ introduction and increasing the temperature to 150 °C, a significant decrease in
702 intensity was observed in all bands except for the one centered at 1620 cm⁻¹, whose complex
703 assignment is discussed above. From this temperature onward, a distinct peak at 1550 cm⁻¹, attributed
704 to bridging bidentate carbonates, emerged. The sequential incorporation of Ru after Ba (configuration
705 V in Figure 10) enhanced hydrogen mobility at the Ru active sites via the spillover effect. The good
706 dispersion of basic-adsorption sites and Ru catalytically active sites in high surface and porous
707 support yield to an enhanced DFM performance as Tsiotsias et al. reported [76]. This promoted a
708 more effective transformation of both low-strength (1620 cm⁻¹) and high-strength (1383 cm⁻¹)
709 bidentate chelated carbonates by breaking the coordination bonds at the BaO-BaO centers. Part of the
710 decomposition of these carbonates led to CH₄ formation, as detected in the gas phase spectra (data
711 not shown), while some evolved into bridged species that were progressively reduced to CH₄ with
712 increasing temperature until disappearing at 500 °C. The persistence of the 1620 cm⁻¹ band even at
713 500 °C supports the formation of adsorbed water subsequent to methanation reaction, as discussed
714 before.

715

716 4. Concluding remarks

717 The study investigates the functionalization of silica with basic components and active Ru to create
718 a dual function material for CO₂ methanation reaction, focusing on the effects of Ba loading and
719 impregnation methods. FT-IR and spectroscopic analyses revealed a heterogeneous surface with
720 silanols, basic oxides, and coordinatively unsaturated Lewis sites that promote CO₂ activation.

721 CO₂ adsorption/desorption studies identified bicarbonate and carbonate species of varying thermal
722 stability, linked to methanation activity. The Ru-16Ba/SiO₂ catalyst favors low-temperature, labile
723 carbonate formation by placing Ru atop Ba, enhancing CO₂ storage and avoiding active phase
724 blockage. Higher Ba loading generates stronger, high-temperature carbonates requiring more heat for
725 CH₄ conversion. Surface CO adsorption studies indicate that basic oxides support electron donation
726 to Ru, stabilizing Ru particles under reaction conditions.

727 The study established a clear relationship between the material's composition and its performance.
728 Furthermore, the sequence in which the components were impregnated proved critical. While the
729 overall CO₂ storage capacity remained largely unaffected at lower Ba concentrations, the preparation
730 order strongly dictated the nature, strength, and regenerability of the adsorbed carbonates. This
731 impregnation sequence also played a key role in positioning the Ruthenium (Ru) methanation
732 catalyst, thereby influencing both the CO₂ conversion activity and the reactivity of the captured
733 carbonate species.

734 Ultimately, a significant finding was the distinct behavior of SiO₂ support compared to conventional
735 alumina-based systems. The non-interacting nature of the silica support provided an advantage by
736 favoring lower-temperature regeneration, which is beneficial for the overall energy efficiency of the
737 cyclic process. Through detailed structural and surface analyses, the research successfully correlated
738 the formation of specific carbonate populations with the synthesis variables, providing new
739 mechanistic insights. In summary, the work validates mesoporous silica as a viable, tunable, and
740 highly effective support for DFMs, advancing the design of materials tailored for integrated CO₂
741 capture and methanation technology.

742

743 **Acknowledgments**

744 Drs. SMR, MDV, and LV are grateful for the financial support of Piano Nazionale di Ripresa e
745 Resilienza funded by the Italian Ministry of University and research (MUR), in the framework of the

746 European Union - NextGenerationEU - Mission 4 "Education and Research", PRIN 2022 PNRR
 747 SILCO-TITOLO (P2022SZANL) Project"

748 **Founding Sources**

749 This work has been performed under the financial support of Piano Nazionale di Ripresa e Resilienza
 750 funded by the Italian Ministry of University and Research (MUR), in the framework of the European
 751 Union - NextGenerationEU - Mission 4 "Education and Research", PRIN 2022 PNRR SILCO-
 752 TITOLO (P2022SZANL) Project"

753

754 **References**

- 755 [1] Rebecca Lindsey, Climate change: atmospheric carbon dioxide, Climate.Gov (NOAA) (2025).
 756 [https://www.climate.gov/news-features/understanding-climate/climate-change-atmospheric-carbon-](https://www.climate.gov/news-features/understanding-climate/climate-change-atmospheric-carbon-dioxide)
 757 [dioxide](https://www.climate.gov/news-features/understanding-climate/climate-change-atmospheric-carbon-dioxide) (accessed July 28, 2025).
- 758 [2] K. Calvin, D. Dasgupta, G. Krinner, A. Mukherji, P.W. Thorne, C. Trisos, J. Romero, P. Aldunce, K.
 759 Barrett, G. Blanco, W.W.L. Cheung, S. Connors, F. Denton, A. Diongue-Niang, D. Dodman, M.
 760 Garschagen, O. Geden, B. Hayward, C. Jones, F. Jotzo, T. Krug, R. Lasco, Y.-Y. Lee, V. Masson-
 761 Delmotte, M. Meinshausen, K. Mintenbeck, A. Mokssit, F.E.L. Otto, M. Pathak, A. Pirani, E.
 762 Poloczanska, H.-O. Pörtner, A. Revi, D.C. Roberts, J. Roy, A.C. Ruane, J. Skeea, P.R. Shukla, R. Slade,
 763 A. Slangen, Y. Sokona, A.A. Sörensson, M. Tignor, D. van Vuuren, Y.-M. Wei, H. Winkler, P. Zhai,
 764 Z. Zommers, J.-C. Hourcade, F.X. Johnson, S. Pachauri, N.P. Simpson, C. Singh, A. Thomas, E. Totin,
 765 A. Alegría, K. Armour, B. Bednar-Friedl, K. Blok, G. Cissé, F. Dentener, S. Eriksen, E. Fischer, G.
 766 Garner, C. Guivarch, M. Haasnoot, G. Hansen, M. Hauser, E. Hawkins, T. Hermans, R. Kopp, N.
 767 Leprince-Ringuet, J. Lewis, D. Ley, C. Ludden, L. Niamir, Z. Nicholls, S. Some, S. Szopa, B. Trewin,
 768 K.-I. van der Wijst, G. Winter, M. Witting, A. Birt, M. Ha, IPCC, 2023: Climate Change 2023:
 769 Synthesis Report. Contribution of Working Groups I, II and III to the Sixth Assessment Report of the
 770 Intergovernmental Panel on Climate Change [Core Writing Team, H. Lee and J. Romero (eds.)]. IPCC,
 771 Geneva, Switzerland., 2023. <https://doi.org/10.59327/IPCC/AR6-9789291691647>.
- 772 [3] P.A. Saenz Cavazos, E. Hunter-Sellars, P. Iacomi, S.R. McIntyre, D. Danaci, D.R. Williams,
 773 Evaluating solid sorbents for CO2 capture: linking material properties and process efficiency via
 774 adsorption performance, *Front. Energy Res.* 11 (2023). <https://doi.org/10.3389/fenrg.2023.1167043>.
- 775 [4] H. Zentou, B. Hoque, M.A. Abdalla, A.F. Saber, O.Y. Abdelaziz, M. Aliyu, A.M. Alkhedhair, A.J.
 776 Alabduly, M.M. Abdelnaby, Recent advances and challenges in solid sorbents for CO2 capture, *Carbon*
 777 *Capture Science & Technology* 15 (2025) 100386. <https://doi.org/10.1016/j.ccst.2025.100386>.
- 778 [5] NOAA Research, No sign of greenhouse gases increases slowing in 2023, (2024).
 779 <https://research.noaa.gov/no-sign-of-greenhouse-gases-increases-slowng-in-2023/> (accessed July 28,
 780 2025).
- 781 [6] Y. Wang, L. Zhao, A. Otto, M. Robinius, D. Stolten, A Review of Post-combustion CO2 Capture
 782 Technologies from Coal-fired Power Plants, *Energy Procedia* 114 (2017) 650–665.
 783 <https://doi.org/10.1016/j.egypro.2017.03.1209>.

- 784 [7] F. Raganati, F. Miccio, P. Ammendola, Adsorption of Carbon Dioxide for Post-combustion Capture:
785 A Review, *Energy & Fuels* 35 (2021) 12845–12868. <https://doi.org/10.1021/acs.energyfuels.1c01618>.
- 786 [8] S. Molina-Ramírez, D. Peltzer, M. Cortés-Reyes, C. Herrera, M.A. Larrubia, L. Cornaglia, L.J.
787 Alemany, CO₂-SR technology using NiBa unsupported catalyst. Isotopic study of cyclic process of
788 CO₂ storage and in situ regeneration with CH₄, *Fuel* 341 (2023) 127690.
789 <https://doi.org/10.1016/j.fuel.2023.127690>.
- 790 [9] A. Porta, C. Larghi, L. Lietti, C.G. Visconti, Once-through CO₂ hydrogenation to grid-compatible
791 synthetic natural gas over a Ru-based catalyst at atmospheric pressure, *Catal. Today* 442 (2024)
792 114907. <https://doi.org/10.1016/j.cattod.2024.114907>.
- 793 [10] P. Frontera, A. Macario, M. Ferraro, P.L. Antonucci, Supported catalysts for CO₂ methanation: A
794 review, *Catalysts* 7 (2017). <https://doi.org/10.3390/catal7020059>.
- 795 [11] C. Shen, M. Liu, S. He, H. Zhao, C. Liu, Advances in the studies of the supported ruthenium catalysts
796 for CO₂ methanation, *Chinese Journal of Catalysis* 63 (2024) 1–15. [https://doi.org/10.1016/S1872-
797 2067\(24\)60090-2](https://doi.org/10.1016/S1872-2067(24)60090-2).
- 798 [12] A.B. Rao, E.S. Rubin, A Technical, Economic, and Environmental Assessment of Amine-Based CO₂
799 Capture Technology for Power Plant Greenhouse Gas Control, *Environ. Sci. Technol.* 36 (2002) 4467–
800 4475. <https://doi.org/10.1021/es0158861>.
- 801 [13] M.S. Duyar, M.A.A. Treviño, R.J. Farrauto, Dual function materials for CO₂ capture and conversion
802 using renewable H₂, *Appl. Catal. B* 168–169 (2015) 370–376.
803 <https://doi.org/10.1016/j.apcatb.2014.12.025>.
- 804 [14] R.J.; D.M.S.; P.A.A. Farrauto, *Methods, Systems, and Materials for Capturing Carbon Dioxide and
805 Converting it to a Chemical Product*, WO2016/007825A1, 2016.
- 806 [15] C. Jeong-Potter, M. Abdallah, S. Kota, R. Farrauto, Enhancing the CO₂ Adsorption Capacity of γ -Al₂
807 O₃ Supported Alkali and Alkaline-Earth Metals: Impacts of Dual Function Material (DFM) Preparation
808 Methods, *Ind. Eng. Chem. Res.* 61 (2022) 10474–10482. <https://doi.org/10.1021/acs.iecr.2c00364>.
- 809 [16] A. Porta, C.G. Visconti, L. Castoldi, R. Matarrese, C. Jeong-Potter, R. Farrauto, L. Lietti, Ru-Ba
810 synergistic effect in dual functioning materials for cyclic CO₂ capture and methanation, *Appl. Catal. B*
811 283 (2021) 119654. <https://doi.org/10.1016/J.APCATB.2020.119654>.
- 812 [17] G. Nava, A. Porta, C.G. Visconti, R. Matarrese, Impact of sorbent-catalyst layouts on Ru/K-based
813 DFMs for integrated CO₂ capture and methanation, *Appl. Catal. A Gen.* 709 (2026) 120654.
814 <https://doi.org/10.1016/j.apcata.2025.120654>.
- 815 [18] M.A. Arellano-Treviño, Z. He, M.C. Libby, R.J. Farrauto, Catalysts and adsorbents for CO₂ capture
816 and conversion with dual function materials: Limitations of Ni-containing DFMs for flue gas
817 applications, *Journal of CO₂ Utilization* 31 (2019) 143–151.
818 <https://doi.org/10.1016/j.jcou.2019.03.009>.
- 819 [19] C. Jeong-Potter, A. Porta, R. Matarrese, C.G. Visconti, L. Lietti, R. Farrauto, Aging study of low Ru
820 loading dual function materials (DFM) for combined power plant effluent CO₂ capture and
821 methanation, *Appl. Catal. B* 310 (2022) 121294. <https://doi.org/10.1016/j.apcatb.2022.121294>.
- 822 [20] A. Bermejo-López, B. Pereda-Ayo, J.A. Onrubia-Calvo, J.A. González-Marcos, J.R. González-
823 Velasco, Aging studies on dual function materials Ru/Ni-Na/Ca-Al₂O₃ for CO₂ adsorption and
824 hydrogenation to CH₄, *J. Environ. Chem. Eng.* 10 (2022) 107951.
825 <https://doi.org/10.1016/j.jece.2022.107951>.

- 826 [21] S. Cimino, F. Boccia, L. Lisi, Effect of alkali promoters (Li, Na, K) on the performance of Ru/Al₂O₃
827 catalysts for CO₂ capture and hydrogenation to methane, *Journal of CO₂ Utilization* 37 (2020) 195–
828 203. <https://doi.org/10.1016/j.jcou.2019.12.010>.
- 829 [22] A. Porta, R. Matarrese, C.G. Visconti, L. Castoldi, L. Lietti, Storage Material Effects on the
830 Performance of Ru-Based CO₂ Capture and Methanation Dual Functioning Materials, *Ind. Eng. Chem.*
831 *Res.* 60 (2021) 6706–6718. <https://doi.org/10.1021/acs.iecr.0c05898>.
- 832 [23] M.S. Duyar, S. Wang, M.A. Arellano-Treviño, R.J. Farrauto, CO₂ utilization with a novel dual
833 function material (DFM) for capture and catalytic conversion to synthetic natural gas: An update,
834 *Journal of CO₂ Utilization* 15 (2016) 65–71. <https://doi.org/10.1016/j.jcou.2016.05.003>.
- 835 [24] S. Essounani-Mérida, S. Molina-Ramírez, M. Cortés-Reyes, C. Herrera, M.Á. Larrubia, L.J. Alemany,
836 Influence of second metal incorporation on nickel-based unsupported catalysts for CO₂ reduction
837 (CO₂-SR) Technology, *Results in Engineering* 26 (2025) 104921.
838 <https://doi.org/10.1016/j.rineng.2025.104921>.
- 839 [25] A. Porta, C.G. Visconti, L. Castoldi, R. Matarrese, C. Jeong-Potter, R. Farrauto, L. Lietti, Ru-Ba
840 synergistic effect in dual functioning materials for cyclic CO₂ capture and methanation, *Appl. Catal. B*
841 283 (2021) 119654. <https://doi.org/10.1016/j.apcatb.2020.119654>.
- 842 [26] A. Bermejo-López, B. Pereda-Ayo, J.A. Onrubia-Calvo, J.A. González-Marcos, J.R. González-
843 Velasco, How the presence of O₂ and NO_x influences the alternate cycles of CO₂ adsorption and
844 hydrogenation to CH₄ on Ru-Na-Ca/Al₂O₃ dual function material, *Journal of CO₂ Utilization* 67
845 (2023) 102343. <https://doi.org/10.1016/j.jcou.2022.102343>.
- 846 [27] J.A. Onrubia-Calvo, A. Bermejo-López, S. Pérez-Vázquez, B. Pereda-Ayo, J.A. González-Marcos, J.R.
847 González-Velasco, Applicability of LaNiO₃-derived catalysts as dual function materials for CO₂
848 capture and in-situ conversion to methane, *Fuel* 320 (2022) 123842.
849 <https://doi.org/10.1016/J.FUEL.2022.123842>.
- 850 [28] J.A. Onrubia-Calvo, B. Pereda-Ayo, J.A. González-Marcos, J.R. González-Velasco, Lanthanum partial
851 substitution by basic cations in LaNiO₃/CeO₂ precursors to raise DFM performance for integrated CO₂
852 capture and methanation, *Journal of CO₂ Utilization* 81 (2024) 102704.
853 <https://doi.org/10.1016/J.JCOU.2024.102704>.
- 854 [29] E. Bracciotti, D. Salusso, I. López-Luque, S. Bertinetti, L.A. Luque-Álvarez, L.F. Bobadilla, G. Prieto,
855 M. Moliner, S. Bordiga, S. Rojas-Buzo, Structural and electronic modulation by Ce-doping in MOF-
856 derived In₂O₃@CeO₂-ZrO₂ catalysts for CO₂ hydrogenation, *Chemical Engineering Journal* 527
857 (2026) 171706. <https://doi.org/10.1016/j.cej.2025.171706>.
- 858 [30] L.-P. Merkouri, J.L. Martín-Espejo, L.F. Bobadilla, J.A. Odriozola, M.S. Duyar, T.R. Reina, Flexible
859 NiRu Systems for CO₂ Methanation: From Efficient Catalysts to Advanced Dual-Function Materials,
860 *Nanomaterials* 13 (2023) 506. <https://doi.org/10.3390/nano13030506>.
- 861 [31] S. Bahrami Gharamaleki, S. Carrasco Ruiz, T. Ramirez Reina, M. Short, M.S. Duyar, Effect of
862 adsorbent loading on NaNiRu-DFMs' CO₂ capture and methanation: finding optimal Na-loading using
863 Bayesian optimisation guided experiments, *Industrial Chemistry & Materials* (2026).
864 <https://doi.org/10.1039/D5IM00019J>.
- 865 [32] S. Cimino, E.M. Cepollaro, L. Lisi, On the effect of Li or Na doping on Ru/TiO₂ catalyst for CO₂
866 methanation, *Catal. Today* 452 (2025) 115245. <https://doi.org/10.1016/j.cattod.2025.115245>.
- 867 [33] W. Zhang, H. Lin, Y. Wei, X. Zhou, Y. An, Y. Dai, Q. Niu, T. Lin, L. Zhong, Overturning CO₂
868 Hydrogenation Selectivity via Strong Metal–Support Interaction, *ACS Catal.* 14 (2024) 2409–2417.
869 <https://doi.org/10.1021/acscatal.3c05527>.

- 870 [34] Y. Li, Z. Liu, Z. Rao, F. Yu, W. Bao, Y. Tang, H. Zhao, J. Zhang, Z. Wang, J. Li, Z. Huang, Y. Zhou,
871 Y. Li, B. Dai, Experimental and theoretical insights into an enhanced CO₂ methanation mechanism
872 over a Ru-based catalyst, *Appl. Catal. B* 319 (2022) 121903.
873 <https://doi.org/10.1016/j.apcatb.2022.121903>.
- 874 [35] J. Ilsemann, M.M. Murshed, T.M. Gesing, J. Kopyscinski, M. Bäumer, On the support dependency of
875 the CO₂ methanation – decoupling size and support effects, *Catal. Sci. Technol.* 11 (2021) 4098–4114.
876 <https://doi.org/10.1039/D1CY00399B>.
- 877 [36] M. Mihet, M. Dan, L. Barbu-Tudoran, M.D. Lazar, CO₂ Methanation Using Multimodal Ni/SiO₂
878 Catalysts: Effect of Support Modification by MgO, CeO₂, and La₂O₃, *Catalysts* 11 (2021) 443.
879 <https://doi.org/10.3390/catal11040443>.
- 880 [37] A.A.A. Mohammed, P. Ebrahimi, A. Yuda, M.J. Al-Marri, A. Kumar, M. Ali, H.S. Saad, Role of Ca
881 in Ni-Ca/Fumed-SiO₂ Catalysts for CO₂ Catalytic Conversion to Methane, *Top. Catal.* 68 (2025)
882 1003–1016. <https://doi.org/10.1007/s11244-024-02010-x>.
- 883 [38] M.A. Arellano-Treviño, Z. He, M.C. Libby, R.J. Farrauto, Catalysts and adsorbents for CO₂ capture
884 and conversion with dual function materials: Limitations of Ni-containing DFMs for flue gas
885 applications, *Journal of CO₂ Utilization* 31 (2019) 143–151.
886 <https://doi.org/10.1016/j.jcou.2019.03.009>.
- 887 [39] G. Bergeret, P. Gallezot, Particle Size and Dispersion Measurements, in: *Handbook of Heterogeneous*
888 *Catalysis*, Wiley, 2008: pp. 738–765. <https://doi.org/10.1002/9783527610044.hetcat0038>.
- 889 [40] L.M. Bravo, F.C. Meunier, J. Kopyscinski, Rare earth oxide promoted Ru/Al₂O₃ dual function
890 materials for CO₂ capture and methanation: An operando DRIFTS and TGA study, *Applied Catalysis*
891 *B: Environment and Energy* 361 (2025) 124591. <https://doi.org/10.1016/j.apcatb.2024.124591>.
- 892 [41] S. Bahrami Gharamaleki, S. Carrasco Ruiz, T. Ramirez Reina, M. Short, M.S. Duyar, Effect of
893 adsorbent loading on NaNiRu-DFMs' CO₂ capture and methanation: finding optimal Na-loading using
894 Bayesian optimisation guided experiments, *Industrial Chemistry & Materials* (2026).
895 <https://doi.org/10.1039/D5IM00019J>.
- 896 [42] M. Thommes, K. Kaneko, A. V. Neimark, J.P. Olivier, F. Rodriguez-Reinoso, J. Rouquerol, K.S.W.
897 Sing, Physisorption of gases, with special reference to the evaluation of surface area and pore size
898 distribution (IUPAC Technical Report), *Pure and Applied Chemistry* 87 (2015) 1051–1069.
899 <https://doi.org/10.1515/pac-2014-1117>.
- 900 [43] T. Oliveira Cabral, F. Bellot Noronha, F. Souza Toniolo, Kinetic and DRIFTS studies of the CO₂
901 catalytic hydrogenation on Ru/SiO₂: A comprehensive and strategic investigation of CO₂ methanation
902 mechanisms by kinetic modeling and data regression, *Chemical Engineering Journal* 485 (2024)
903 149716. <https://doi.org/10.1016/j.cej.2024.149716>.
- 904 [44] A. Infantes-Molina, L. Righini, L. Castoldi, C.V. Loricera, J.L.G. Fierro, A. Sin, L. Lietti,
905 Characterization and reactivity of Ce-promoted PtBa lean NO_x trap catalysts, *Catal. Today* 197 (2012)
906 178–189. <https://doi.org/10.1016/j.cattod.2012.07.036>.
- 907 [45] G. Busca, Infrared (IR) Spectroscopy, in: *Springer Handbook of Advanced Catalyst Characterization*,
908 2023: pp. 3–32. https://doi.org/10.1007/978-3-031-07125-6_1.
- 909 [46] L.M.F. Lopes, L.M. Ilharco, Hydrofluoric acid-induced fluorination and formation of silica
910 nanocapsules for ¹⁹F magnetic resonance imaging, *RSC Adv.* 4 (2014) 16931–16934.
911 <https://doi.org/10.1039/C3RA47842D>.

- 912 [47] G. Busca, V. Lorenzelli, Infrared spectroscopic identification of species arising from reactive
913 adsorption of carbon oxides on metal oxide surfaces, *Materials Chemistry* 7 (1982) 89–126.
914 [https://doi.org/10.1016/0390-6035\(82\)90059-1](https://doi.org/10.1016/0390-6035(82)90059-1).
- 915 [48] G. Ramis, G. Busca, V. Lorenzelli, Low-temperature CO₂ adsorption on metal oxides: spectroscopic
916 characterization of some weakly adsorbed species, *Mater. Chem. Phys.* 29 (1991) 425–435.
917 [https://doi.org/10.1016/0254-0584\(91\)90037-U](https://doi.org/10.1016/0254-0584(91)90037-U).
- 918 [49] G. Busca, Catalytic materials based on silica and alumina: Structural features and generation of surface
919 acidity, *Prog. Mater. Sci.* 104 (2019) 215–249. <https://doi.org/10.1016/j.pmatsci.2019.04.003>.
- 920 [50] G. Busca, Spectroscopic characterization of the acid properties of metal oxide catalysts, *Catal. Today*
921 41 (1998) 191–206. [https://doi.org/10.1016/S0920-5861\(98\)00049-2](https://doi.org/10.1016/S0920-5861(98)00049-2).
- 922 [51] G. Busca, The surface acidity of solid oxides and its characterization by IR spectroscopic methods. An
923 attempt at systematization, *Physical Chemistry Chemical Physics* 1 (1999) 723–736.
924 <https://doi.org/10.1039/a808366e>.
- 925 [52] G. Garbarino, D. Bellotti, E. Finocchio, L. Magistri, G. Busca, Methanation of carbon dioxide on
926 Ru/Al₂O₃: Catalytic activity and infrared study, *Catal. Today* 277 (2016) 21–28.
927 <https://doi.org/10.1016/j.cattod.2015.12.010>.
- 928 [53] P.A. Kots, T. Xie, B.C. Vance, C.M. Quinn, M.D. de Mello, J.A. Boscoboinik, C. Wang, P. Kumar,
929 E.A. Stach, N.S. Marinkovic, L. Ma, S.N. Ehrlich, D.G. Vlachos, Electronic modulation of metal-
930 support interactions improves polypropylene hydrogenolysis over ruthenium catalysts, *Nat. Commun.*
931 13 (2022) 5186. <https://doi.org/10.1038/s41467-022-32934-5>.
- 932 [54] K.I. Hadjiivanov, G.N. Vayssilov, Characterization of oxide surfaces and zeolites by carbon monoxide
933 as an IR probe molecule, in: 2002: pp. 307–511. [https://doi.org/10.1016/S0360-0564\(02\)47008-3](https://doi.org/10.1016/S0360-0564(02)47008-3).
- 934 [55] S.Y. Chin, C.T. Williams, M.D. Amiridis, FTIR Studies of CO Adsorption on Al₂O₃- and SiO₂-
935 Supported Ru Catalysts, *J. Phys. Chem. B* 110 (2006) 871–882. <https://doi.org/10.1021/jp053908q>.
- 936 [56] J. Ilsemann, M.M. Murshed, T.M. Gesing, J. Kopyscinski, M. Bäumer, On the support dependency of
937 the CO₂ methanation – decoupling size and support effects, *Catal. Sci. Technol.* 11 (2021) 4098–4114.
938 <https://doi.org/10.1039/D1CY00399B>.
- 939 [57] R.A. Dalla Betta, Carbon monoxide adsorption on supported ruthenium, *J. Phys. Chem.* 79 (1975)
940 2519–2525. <https://doi.org/10.1021/j100590a015>.
- 941 [58] M. Kantcheva, S. Sayan, On the mechanism of CO adsorption on a silica-supported ruthenium catalyst,
942 *Catal. Letters* 60 (1999) 27–38. <https://doi.org/10.1023/A:1019082218590>.
- 943 [59] K. Hadjiivanov, J.-C. Lavalley, J. Lamotte, F. Maugé, J. Saint-Just, M. Che, FTIR Study of CO
944 Interaction with Ru/TiO₂ Catalysts, *J. Catal.* 176 (1998) 415–425.
945 <https://doi.org/10.1006/jcat.1998.2038>.
- 946 [60] F. Frola, F. Prinetto, G. Ghiotti, L. Castoldi, I. Nova, L. Lietti, P. Forzatti, Combined in situ FT-IR and
947 TRM analysis of the NO_x storage properties of Pt-Ba/Al₂O₃ LNT catalysts, *Catal. Today* 126 (2007)
948 81–89. <https://doi.org/10.1016/j.cattod.2006.10.010>.
- 949 [61] F. Prinetto, M. Manzoli, S. Morandi, F. Frola, G. Ghiotti, L. Castoldi, L. Lietti, P. Forzatti, Pt-K/Al₂
950 O₃ NSR Catalysts: Characterization of Morphological, Structural and Surface Properties, *The Journal*
951 *of Physical Chemistry C* 114 (2010) 1127–1138. <https://doi.org/10.1021/jp909026p>.

- 952 [62] F. Frola, M. Manzoli, F. Prinetto, G. Ghiotti, L. Castoldi, L. Lietti, Pt–Ba/Al₂O₃ NSR Catalysts at
953 Different Ba Loading: Characterization of Morphological, Structural, and Surface Properties, *The*
954 *Journal of Physical Chemistry C* 112 (2008) 12869–12878. <https://doi.org/10.1021/jp801480t>.
- 955 [63] L. Castoldi, L. Lietti, I. Nova, R. Matarrese, P. Forzatti, F. Vindigni, S. Morandi, F. Prinetto, G. Ghiotti,
956 Alkaline- and alkaline-earth oxides based Lean NO_x Traps: Effect of the storage component on the
957 catalytic reactivity, *Chemical Engineering Journal* 161 (2010) 416–423.
958 <https://doi.org/10.1016/j.cej.2009.10.065>.
- 959 [64] A. Porta, R. Matarrese, C.G. Visconti, L. Lietti, Spatially resolved insights from operando FT-IR on
960 integrated CO₂ capture and hydrogenation in the presence of NO_x, *Chemical Engineering Journal* 521
961 (2025) 166577. <https://doi.org/10.1016/j.cej.2025.166577>.
- 962 [65] C. Jeong-Potter, M. Abdallah, S. Kota, R. Farrauto, Enhancing the CO₂ Adsorption Capacity of γ -Al₂
963 O₃ Supported Alkali and Alkaline-Earth Metals: Impacts of Dual Function Material (DFM) Preparation
964 Methods, *Ind. Eng. Chem. Res.* 61 (2022) 10474–10482. <https://doi.org/10.1021/acs.iecr.2c00364>.
- 965 [66] A. Porta, R. Matarrese, C.G. Visconti, L. Lietti, Investigation of DFMs for CO₂ Capture and
966 Methanation by Coupled Microreactor Experiments and FT-IR Spectroscopy, *Energy & Fuels* 37
967 (2023) 7280–7290. <https://doi.org/10.1021/acs.energyfuels.3c00443>.
- 968 [67] T. Montanari, L. Castoldi, L. Lietti, G. Busca, Basic catalysis and catalysis assisted by basicity: FT-IR
969 and TPD characterization of potassium-doped alumina, *Appl. Catal. A Gen.* 400 (2011) 61–69.
970 <https://doi.org/10.1016/j.apcata.2011.04.016>.
- 971 [68] I. Malpartida, M. Vargas, L. Alemany, E. Finocchio, G. Busca, Pt–Ba–Al₂O₃ for NO_x storage and
972 reduction: Characterization of the dispersed species, *Appl. Catal. B* 80 (2008) 214–225.
973 <https://doi.org/10.1016/j.apcatb.2007.11.035>.
- 974 [69] P. Panagiotopoulou, D.I. Kondarides, Xenophon.E. Verykios, Selective methanation of CO over
975 supported Ru catalysts, *Appl. Catal. B* 88 (2009) 470–478.
976 <https://doi.org/10.1016/j.apcatb.2008.10.012>.
- 977 [70] C.-H. Yeh, H.V. Thang, Y.I.A. Reyes, C. Coluccini, H.-Y.T. Chen, DFT Insights into Hydrogen
978 Spillover Mechanisms: Effects of Metal Species, Size, and Support, *The Journal of Physical Chemistry*
979 *C* 129 (2025) 6185–6195. <https://doi.org/10.1021/acs.jpcc.4c08097>.
- 980 [71] A. Misol, I. Giarnieri, F. Ospitali, A. Ballarini, J. Jiménez-Jiménez, E. Rodríguez-Castellón, F.M.
981 Labajos, G. Fornasari, P. Benito, CO₂ hydrogenation over Ru hydrotalcite-derived catalysts, *Catal.*
982 *Today* 425 (2024) 114362. <https://doi.org/10.1016/j.cattod.2023.114362>.
- 983 [72] X. Wang, Y. Hong, H. Shi, J. Szanyi, Kinetic modeling and transient DRIFTS–MS studies of CO₂
984 methanation over Ru/Al₂O₃ catalysts, *J. Catal.* 343 (2016) 185–195.
985 <https://doi.org/10.1016/j.jcat.2016.02.001>.
- 986 [73] L. Proaño, E. Tello, M.A. Arellano-Trevino, S. Wang, R.J. Farrauto, M. Cobo, In-situ DRIFTS study
987 of two-step CO₂ capture and catalytic methanation over Ru, “Na₂O”/Al₂O₃ Dual Functional Material,
988 *Appl. Surf. Sci.* 479 (2019) 25–30. <https://doi.org/10.1016/j.apsusc.2019.01.281>.
- 989 [74] L. Falbo, C.G. Visconti, L. Lietti, J. Szanyi, The effect of CO on CO₂ methanation over Ru/Al₂O₃
990 catalysts: a combined steady-state reactivity and transient DRIFT spectroscopy study, *Appl. Catal. B*
991 256 (2019) 117791. <https://doi.org/10.1016/j.apcatb.2019.117791>.
- 992 [75] L. Proaño, M.A. Arellano-Treviño, R.J. Farrauto, M. Figueredo, C. Jeong-Potter, M. Cobo, Mechanistic
993 assessment of dual function materials, composed of Ru–Ni, Na₂O/Al₂O₃ and Pt–Ni, Na₂O/Al₂O₃, for

- 994 CO₂ capture and methanation by in-situ DRIFTS, *Appl. Surf. Sci.* 533 (2020) 147469.
995 <https://doi.org/10.1016/j.apsusc.2020.147469>.
- 996 [76] A.I. Tsiotsias, N.D. Charisiou, A.G.S. Hussien, A.A. Dabbawala, V. Sebastian, K. Polychronopoulou,
997 M.A. Goula, CO₂ capture and methanation using Ru/Na₂O/Al₂O₃ dual-function materials: Effect of
998 support synthesis method and Ru load, *J. Environ. Chem. Eng.* 12 (2024) 112712.
999 <https://doi.org/10.1016/j.jece.2024.112712>.
- 1000

Journal Pre-proof

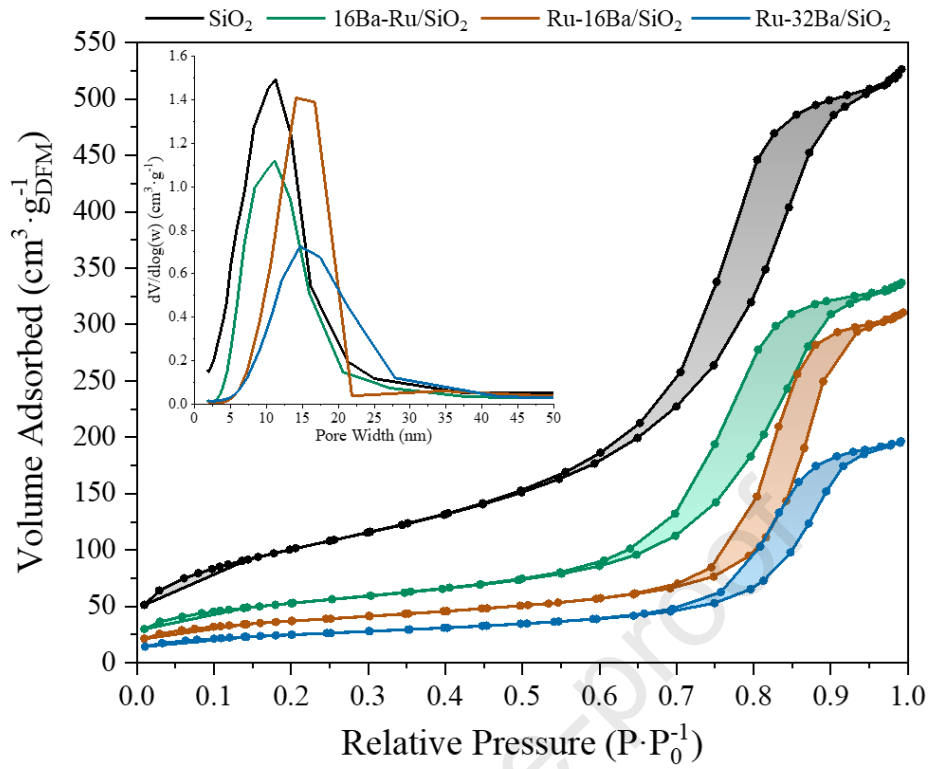


Figure 1. N₂ adsorption-desorption isotherms at 77 K and pore size distribution for the investigated samples.

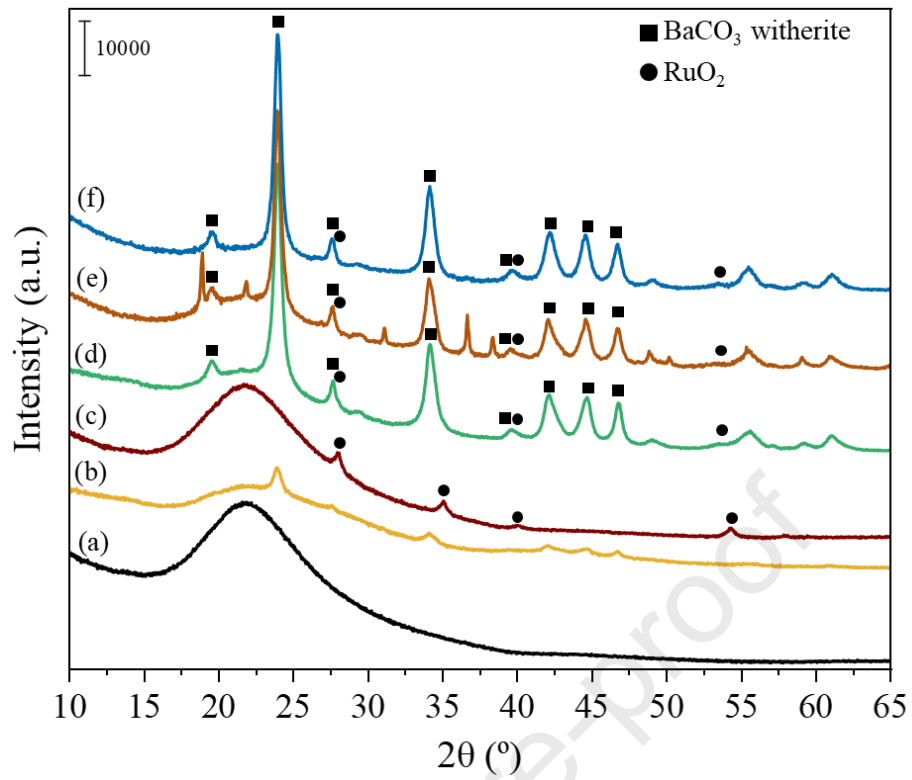


Figure 2. XRD patterns of (a) SiO_2 , (b) $16\text{Ba}/\text{SiO}_2$, (c) Ru/SiO_2 , (d) $16\text{Ba-Ru}/\text{SiO}_2$, (e) $\text{Ru-16Ba}/\text{SiO}_2$ and (f) $\text{Ru-32Ba}/\text{SiO}_2$.

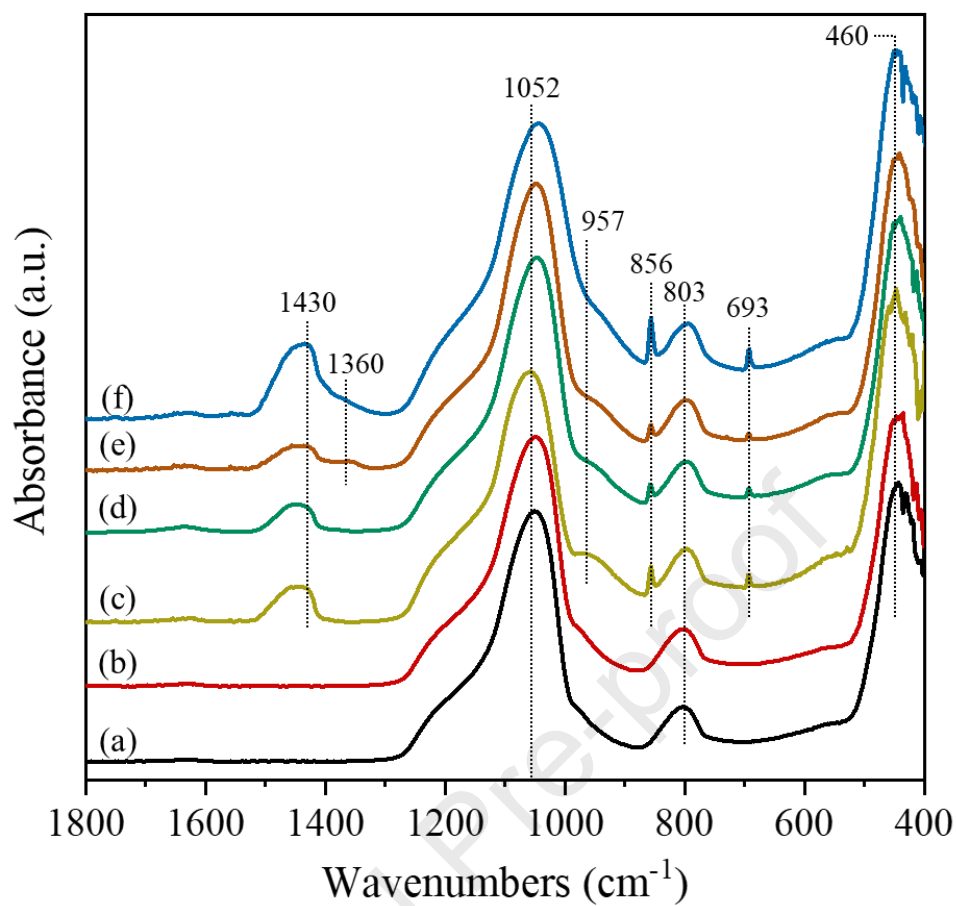


Figure 3. ATR FT-IR spectra of (a) SiO₂, (b) Ru/SiO₂, (c) 16Ba/SiO₂, (d) 16Ba-Ru/SiO₂, (e) Ru-16Ba/SiO₂ and (f) Ru-32Ba/SiO₂.

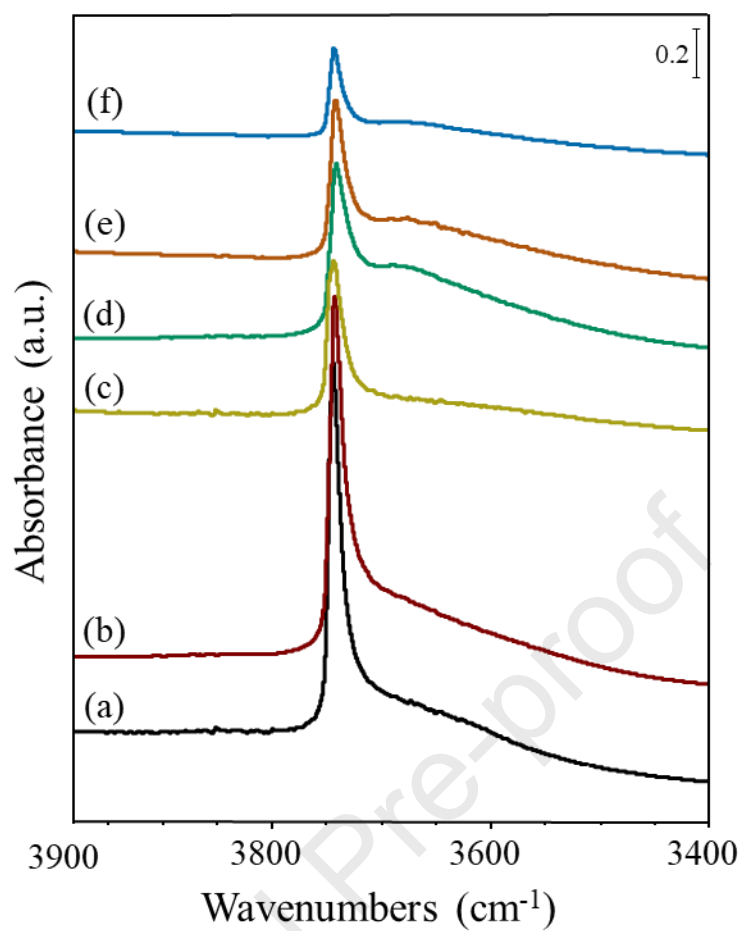


Figure 4. OH stretching region FT-IR spectra of (a) SiO₂, (b) Ru/SiO₂, (c) 16Ba/SiO₂, (d) 16Ba-Ru/SiO₂, (e) Ru-16Ba/SiO₂ and (f) Ru-32Ba/SiO₂ after activation at 500°C for 1 hour.

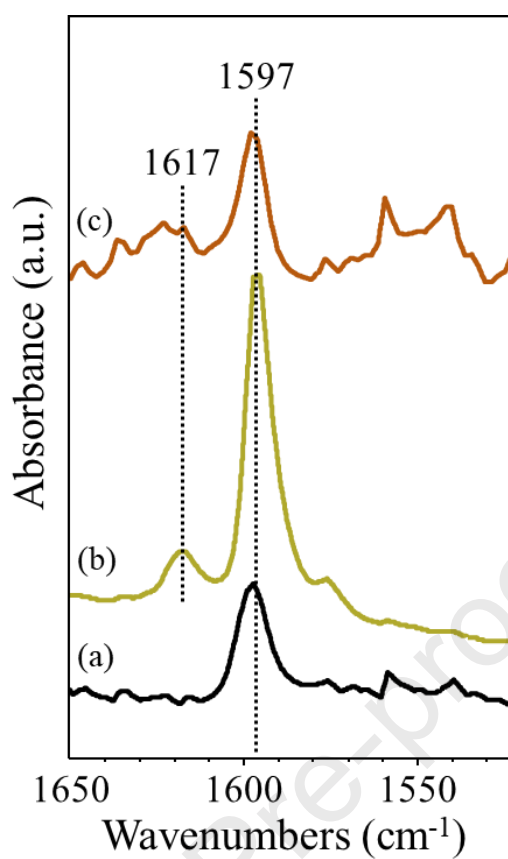


Figure 5. FT-IR subtraction spectra of surface species after desorption of pyridine at 150°C and outgassing at 150°C: (a) SiO₂, (b) 16Ba/SiO₂ and (c) Ru-16Ba/SiO₂(enlarged). The activated spectrum was subtracted.

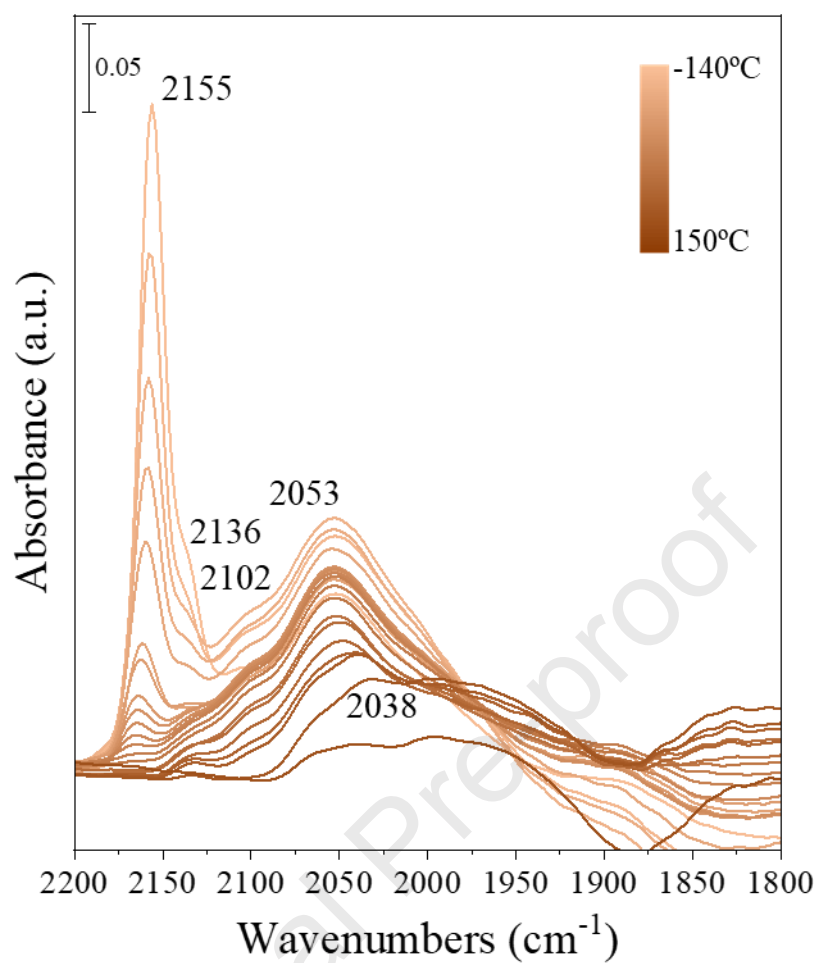


Figure 6. FT-IR spectra of surface species arising from low temperature CO adsorption over Ru-16Ba/SiO₂ and following outgassing from -140°C up to 150°C. The activated surface spectrum was subtracted.

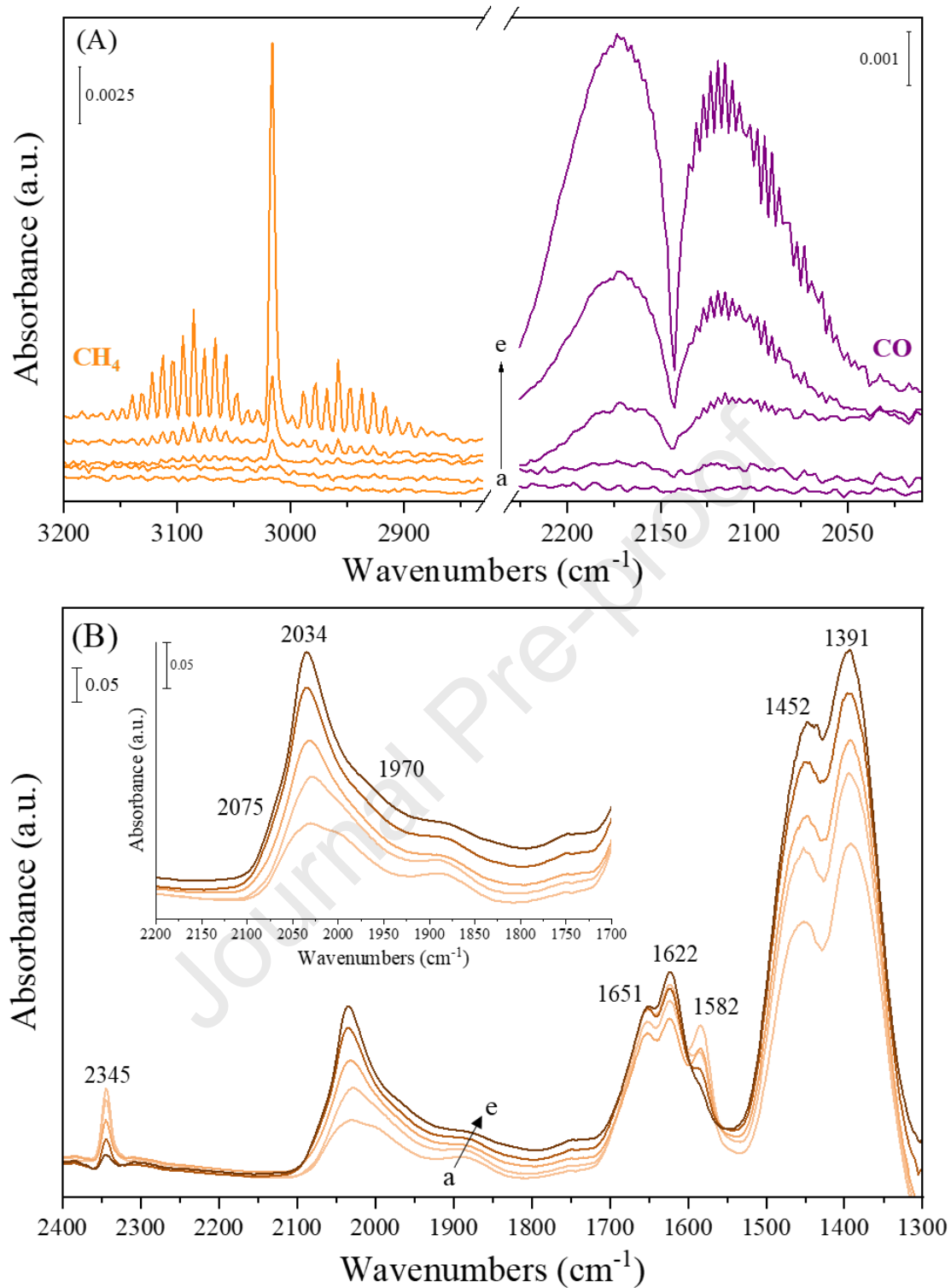


Figure 7. A) gas phase FT-IR spectra and B) surface FT-IR spectra of Ru-16Ba/SiO₂ catalyst in CO₂ + H₂ at increasing temperatures from (a) 200°C to (e) 400°C (50°C/step).

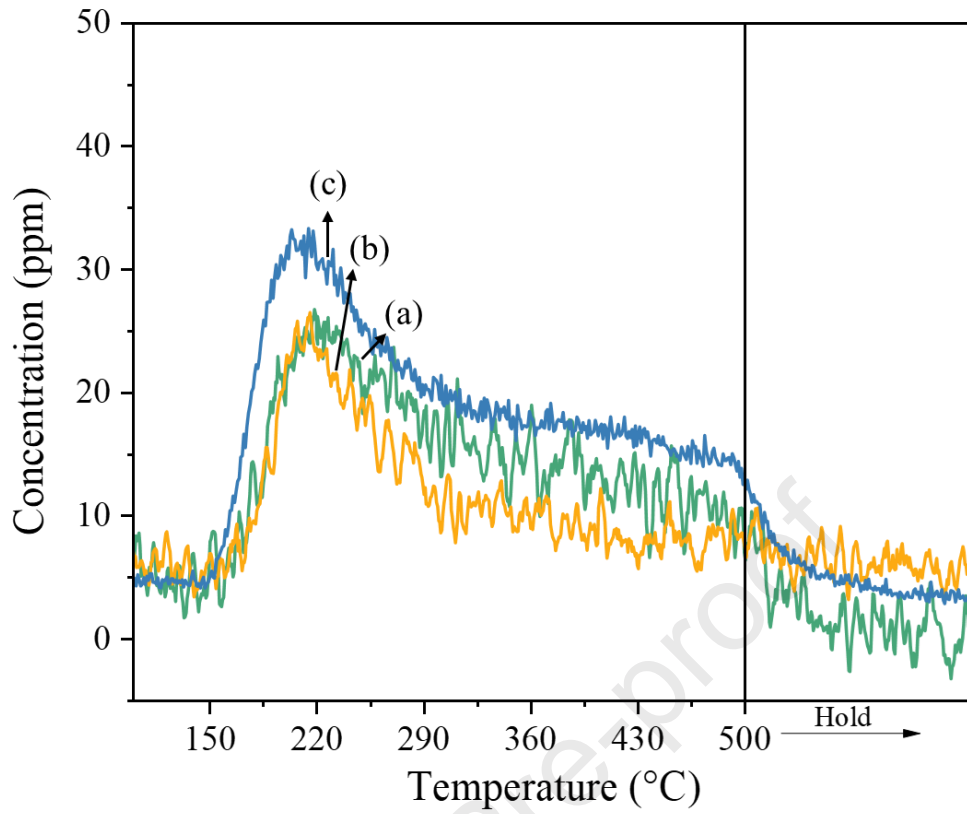


Figure 8. CO₂-TPD profiles for (a) 16Ba-Ru/SiO₂, (b) Ru-16Ba/SiO₂ and (c) Ru-32Ba/SiO₂.

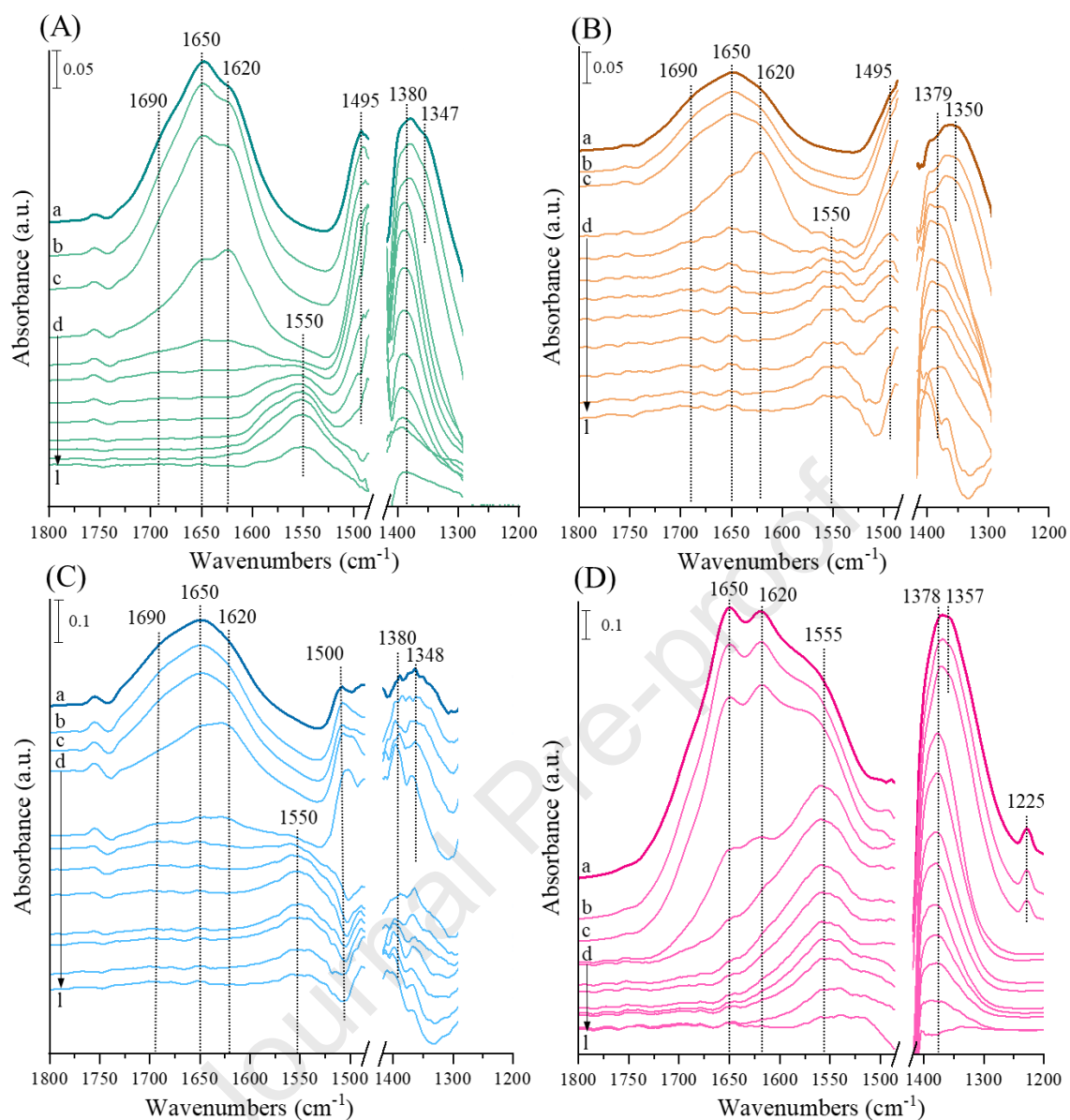


Figure 9. FT-IR spectra of surface species arising from CO₂ adsorption and desorption over (A) 16Ba-Ru/SiO₂ and (B) Ru-16Ba/SiO₂, (C) Ru-32Ba/SiO₂ and (D) 16Ba-Ru/Al₂O₃ at (a) Presence of 18 Torr CO₂ and (b) 2 Torr CO₂ at R.T. (c) outgassing for 2 min and (d) for 1 h at R.T.; outgassing at increasing temperature in 150°C to 500°C (step: 50°C, curves e-l). The spectrum of the activated surface was subtracted.

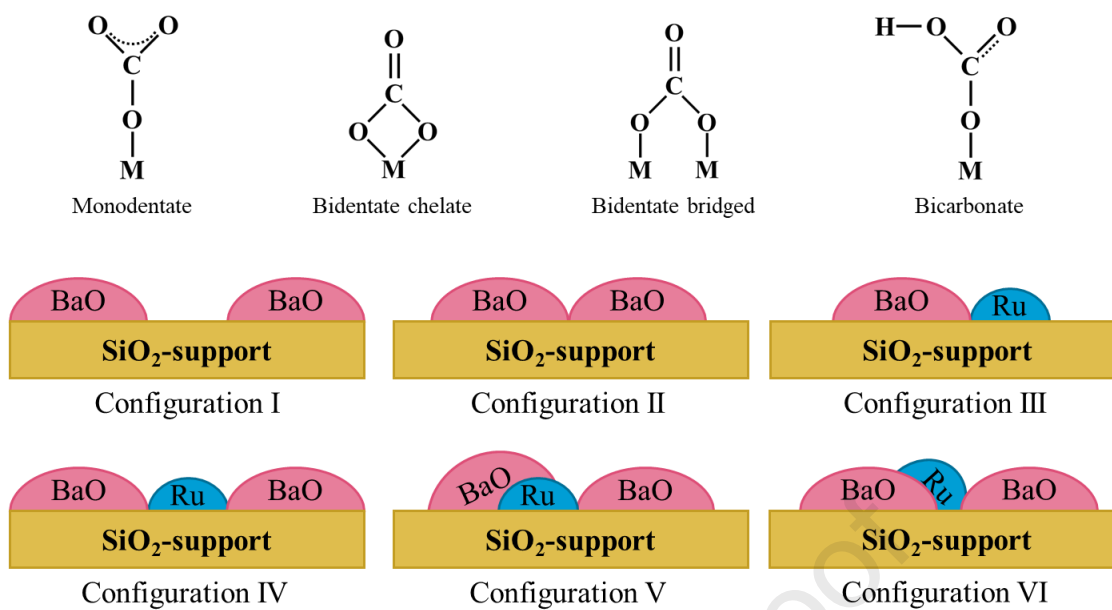


Figure 10. Schematic representation of different carbonate species (M = Metal) and active phase distributions present over silica support.

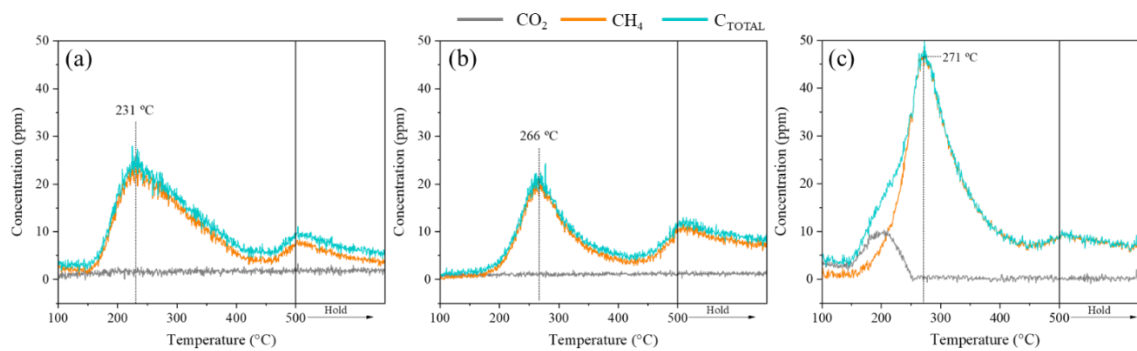


Figure 11. H₂-TPSR profiles for (a) 16Ba-Ru/SiO₂, (b) Ru-16Ba/SiO₂ and (c) Ru-32Ba/SiO₂.

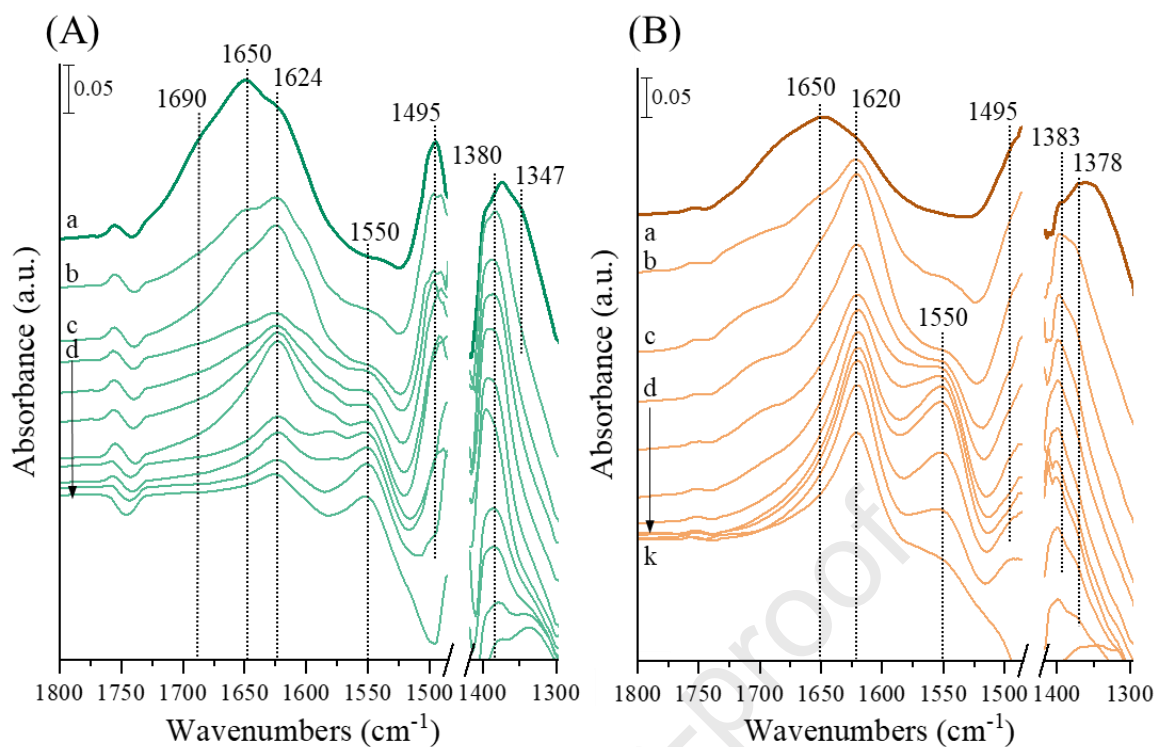


Figure 12. FT-IR spectra of surface species arising from the H₂-TPSR over (A) 16Ba-Ru/SiO₂ and (B) Ru-16Ba/SiO₂ at (a) Presence of 18 Torr CO₂ at R.T., (b) outgassing 1 h at R.T. in the presence of 150 Torr of H₂ at (c) R.T and (d-k) from 150 to 500°C by 50°C/step. The activated spectrum and gas phase spectrum were subtracted.

- Mesoporous silica as support for DFMs to integrate CO₂ capture and methanation
- Ba loading boosts CO₂ storage capacity and carbonate stability
- Ru order impregnation affects methanation activity and carbonate reactivity
- Ru-16Ba/SiO₂ leads to the formation of regenerable carbonates at lower temperatures

Journal Pre-proof

Declaration of interests

The authors declare that they have no known competing financial interests or personal relationships that could have appeared to influence the work reported in this paper.

The authors declare the following financial interests/personal relationships which may be considered as potential competing interests:

Journal Pre-proof